Analytic representation of multi-ion interatomic potentials in transition metals

John A. Moriarty
Lawrence Livermore National Laboratory, University of California, Livermore, California 94550
(Received 20 February 1990)

The first-principles, density-functional version of the generalized pseudopotential theory (GPT), previously developed for empty- and filled-d-band metals, recently has been extended to pure transition metals with partially filled d bands [Phys. Rev. B **38**, 3199 (1988)]. Within this formalism, a rigorous real-space expansion of the bulk total energy has been obtained in terms of widely transferable, *structure-independent* interatomic potentials, including both central-force pair interactions and angular-force triplet and quadruplet interactions. In the central transition metals, the three- and four-ion potentials, v_3 and v_4, are essential to a proper description of materials properties, but are necessarily multidimensional functions which cannot be easily tabulated for application purposes. We develop here a simplified version of the theory, the model GPT, in which these potentials can be expressed *analytically* while retaining the most important physics of the full first-principles treatment. The analytic treatment of v_3 and v_4 is made possible because of three simplifying features in the central transition metals. First, due to the nonspherical nature of the Fermi surface in such metals, the long-range sp-d hybridization tails of the first-principles potentials destructively interfere in total-energy calculations and thus can be dropped at the outset without major consequences. Second, the direct d-d contributions to the potentials are short ranged and need only be retained to fourth order in interatomic d-state matrix elements to obtain a good representation of the d-band-structure energy. Third, the d bands are canonical in nature, with the interatomic matrix elements well approximated by simple forms, so that all remaining low-order d-state contributions can be evaluated analytically. This leads to a description of v_3 and v_4 in terms of universal short-range radial and angular functions. The model GPT is made quantitatively accurate for real materials by allowing the coefficient of each d-state contribution to be adjusted to match first-principles calculations and/or experimental data. In this manner, one can achieve a set of potentials which simultaneously yield a good description of cohesion, vacancy formation, structural phase stability, elastic constants, and phonons, as is demonstrated for the representative case of molybdenum. More generally, the analytic potentials are suitable for widescale applications and permit for the first time the use of the transition-metal GPT in molecular-dynamics and Monte Carlo simulations.

I. INTRODUCTION

Historically, the rigorous development of interatomic potentials from quantum mechanics has been limited to nontransition metals,[1-5] where the presence of weak electron-ion pseudopotentials permit well-defined and rapidly convergent perturbation expansions of the total energy. Working within the framework of *generalized* pseudopotential theory (GPT),[6,7] and Hohenberg-Kohn-Sham local-density-approximation (LDA) quantum mechanics,[8,9] we have recently succeeded in developing a first-principles interatomic-potential expansion of the total energy suitable for transition metals.[10] In the bulk elemental metal with atomic volume Ω, the total-energy functional takes the form

$$E_{\rm tot}(\mathbf{R}_1,\ldots,\mathbf{R}_N)=E_0(\Omega)+\tfrac{1}{2}\sum_{i,j}{}' v_2(i,j)+\tfrac{1}{6}\sum_{i,j,k}{}' v_3(i,j,k)+\tfrac{1}{24}\sum_{i,j,k,l}{}' v_4(i,j,k,l)+\cdots , \quad (1)$$

where the prime on each summation denotes the exclusion of all self-interaction terms where two indices are equal. The leading volume term E_0 in this expansion includes all one-ion *intra-atomic* contributions to the total energy and already leads to a good description of transition-metal cohesion in lowest order. The interatomic potentials v_2, v_3, v_4, etc. are expressible in terms of weak pseudopotential and d-state tight-binding and hybridization matrix elements coupling different sites, and the series is rapidly convergent beyond three-ion interactions. Explicit expressions for E_0, v_2, v_3, and v_4 were derived in Ref. 10 and applied to the $3d$ and $4d$ transition-series metals.

Equation (1) for the total energy is formally analogous to the corresponding expression for nontransition metals, except that in such materials it is usually not necessary to consider higher-order potentials beyond v_2. As in the case of nontransition metals, the interatomic potentials entering Eq. (1) are volume dependent but *structure independent* and thus rigorously transferable at a given volume to all bulk structures, either ordered or disordered. At constant volume Ω, the central-force pair potential v_2 is a one-dimensional function of the ion-ion separation distance $R_{ij}=|\mathbf{R}_i-\mathbf{R}_j|$:

$$v_2(i,j)\equiv v_2(R_{ij};\Omega) , \quad (2)$$

while the angular-force triplet potential v_3 and quadruplet potential v_4 are, respectively, the three- and six-dimensional functions

$$v_3(i,j,k) \equiv v_3(R_{ij}, R_{jk}, R_{ki}; \Omega) \tag{3}$$

and

$$v_4(i,j,k,l) \equiv v_4(R_{ij}, R_{jk}, R_{kl}, R_{li}, R_{ki}, R_{lj}; \Omega) \ . \tag{4}$$

In the full first-principles GPT, the potentials v_2, v_3, and v_4 are all nonanalytic functions with long-range oscillatory tails. Unlike the simple radial function v_2, however, the multidimensional functions v_3 and v_4 cannot be readily tabulated for application purposes and one is forced to recalculate these functions each time they are used. This has greatly inhibited the widespread application of this theory to the central transition metals, where the multi-ion potentials are essential to an accurate description of materials properties. In the present paper we attempt to improve this situation by developing a simplified model transition-metal GPT in which v_3 and v_4 are approximated by analytic short-range forms that retain the dominant physics of the full theory. Central results of the first-principles GPT are reviewed in Sec. II, while the model GPT is developed in Sec. III. In Sec. IV it is then demonstrated how the model GPT can be used to obtain accurate interatomic potentials in the representative case of molybdenum (Mo). We conclude in Sec. V. A preliminary account of portions of this work was reported earlier.[11]

II. FIRST-PRINCIPLES GENERALIZED PSEUDOPOTENTIAL THEORY

The first-principles GPT has been developed completely within the modern framework of LDA quantum mechanics.[7,10] Briefly, both the valence and inner-core electrons in the metal are governed by a one-electron Schrödinger equation,

$$(T+V)|\psi_\alpha\rangle = E_\alpha|\psi_\alpha\rangle \ , \tag{5}$$

where T is the kinetic-energy operator and V is the self-consistent potential. The inner-core electrons are amenable to a purely atomiclike treatment and, invoking the usual small-core approximation, one may transform Eq. (5) to an exactly equivalent pseudo-Schrödinger equation,

$$(T+W)|\phi_\alpha\rangle = E_\alpha|\phi_\alpha\rangle \ , \tag{6}$$

for the remaining s, p, and d valence electrons, where W is an optimized nonlocal pseudopotential operator. For transition metals, W is effectively weak for the nearly-free-electron s and p electrons, just as in simple metals, but is strong for the more localized d electrons. An appropriate basis set with which to represent the valence states in Eq. (6), then, is one consisting of both plane waves $|\mathbf{k}\rangle$ and five *localized* d states $|\phi_d\rangle$ centered on each ion site. The latter are chosen to be exact eigenstates of a suitable atomiclike reference Hamiltonian:

$$(T+v_{\rm at})|\phi_d\rangle = E_d^0|\phi_d\rangle \ . \tag{7}$$

A second effectively weak potential is then

$$\Delta \equiv \delta V - \langle \phi_d|\delta V|\phi_d\rangle \ , \tag{8}$$

where $\delta V \equiv v_{\rm at} - V$. The nearly-free-electron s and p bands are characterized by free-electron energies $\varepsilon_{\mathbf{k}}$ and small plane-wave matrix elements $W_{\mathbf{k}\mathbf{k}'} \equiv \langle \mathbf{k}|W|\mathbf{k}'\rangle$, while the tight-binding-like d bands are characterized by a mean energy

$$E_d \equiv \langle \phi_d|(T+V)|\phi_d\rangle = E_d^0 - \langle \phi_d|\delta V|\phi_d\rangle \tag{9}$$

plus small and short-ranged d-state overlap matrix elements

$$S_{dd'}(R_{ij}) \equiv \langle \phi_d(\mathbf{r}-\mathbf{R}_i)|\phi_{d'}(\mathbf{r}-\mathbf{R}_j)\rangle \tag{10}$$

and

$$\Delta_{dd'}(R_{ij}) \equiv \langle \phi_d(\mathbf{r}-\mathbf{R}_i)|\Delta|\phi_{d'}(\mathbf{r}-\mathbf{R}_j)\rangle \ . \tag{11}$$

The remaining sp-d hybridization between the bands is then described by small plane-wave–d-state matrix elements

$$S_{\mathbf{k}d} \equiv \langle \mathbf{k}|\phi_d\rangle \tag{12}$$

and

$$\Delta_{\mathbf{k}d} \equiv \langle \mathbf{k}|\Delta|\phi_d\rangle \ . \tag{13}$$

The reference system which defines the localized d states $|\phi_d\rangle$ through Eq. (7) and upon which the total-energy expansion (1) is based consists of N isolated transition-metal ions placed in a compensating uniform electron density Z/Ω. Each ion exhibits a strong d resonance in the presence of the free-electron gas such that the number of valence d electrons retained by the ion is

$$Z_d = (10/\pi)\delta_2(\varepsilon_F) \ , \tag{14}$$

where δ_2 is the $l=2$ phase shift of the ion potential and ε_F is the Fermi energy of the free-electron gas:

$$\varepsilon_F = \frac{\hbar^2}{2m}\left[\frac{3\pi^2 Z}{\Omega}\right]^{2/3} \ . \tag{15}$$

For a pure transition metal, Z effectively represents the number of non-d valence electrons per atom and one must additionally require that

$$Z + Z_d = Z_a - Z_c \ , \tag{16}$$

where Z_a is the atomic number and Z_c the number of inner-core electrons per atom for the element in question. Thus, for example, in the case of group-VI*B* elements (Cr, Mo, and W), $Z+Z_d=6$. Equations (14)–(16) then constitute three equations in three unknowns and must be iterated to yield self-consistent values of Z, Z_d, and ε_F. We call the resulting entity, self-consistent ion plus compensation free-electron gas, a "zeroth-order pseudoatom," and the reference system of N neutral zeroth-order pseudoatoms represents an excellent first approximation to a real transition metal. (See, for example, Figs. 3–7 and surrounding discussion of Ref. 10.) In particular, the zeroth-order pseudoatom values of Z and Z_d are

already in good accord with estimates of these quantities from self-consistent band-structure calculations. For the $3d$ and $4d$ transition metals at normal density, Z takes on values in the narrow range $1.1 \leq Z \leq 1.7$, with a typical value of 1.4. For a given element as a function of volume, Z and Z_d also properly reflect any transfer of electrons in or out of the d states, so that for the early and central transition metals (e.g., Mo) Z decreases with compression, representing an $s \rightarrow d$ electron transfer, while for late transition metals (e.g., Cu) Z increases with compression, representing a $d \rightarrow s$ electron transfer. In addition, all elementary aspects of the electronic structure, including the position E_d and width W_d of the d bands, can be accurately estimated from the properties of the pseudoatom. A slight generalization in the pseudoatom definition even allows one to match first-principles band-theory values of Z_d and W_d exactly, if desired. This latter technical refinement is discussed in Appendix A and is used in the present applications to Mo discussed in Secs. III and IV.

The mathematical link between Eqs. (14)–(16) and the localized d states $|\phi_d\rangle$ is established by defining the reference potential $v_{\rm at}$ in Eq. (7) in terms of the zeroth-order pseudoatom potential [Eq. (A1) of Appendix A] and then expressing the phase shift δ_2 in the same $|\mathbf{k}\rangle, |\phi_d\rangle$ basis used to describe the solid. From Eqs. (63) and (65) of Ref. 10, one has

$$\delta_2(E) = -\tfrac{1}{5}\mathrm{Im}\sum_d \ln[E - E_d^{\rm vol} - \Gamma_{dd}^{\rm vol}(E)] , \tag{17}$$

where $\Gamma_{dd}^{\rm vol}$ is the one-ion d-state self-energy

$$\Gamma_{dd}^{\rm vol}(E) \equiv \sum_{\mathbf{k}} \frac{v'_{d\mathbf{k}} v'_{\mathbf{k}d}}{E - \varepsilon_{\mathbf{k}}} , \tag{18}$$

with

$$v'_{\mathbf{k}d} \equiv -(E - E_d^{\rm vol}) S_{\mathbf{k}d} - \Delta_{\mathbf{k}d}^{\rm vol} . \tag{19}$$

In Eqs. (17) and (19), the quantities $E_d^{\rm vol}$ and $\Delta_{\mathbf{k}d}^{\rm vol}$ are the dominant volume components of E_d and $\Delta_{\mathbf{k}d}$, respectively. That is,

$$E_d = E_d^{\rm vol} + E_d^{\rm struc} \tag{20}$$

and

$$\Delta_{\mathbf{k}d} = \Delta_{\mathbf{k}d}^{\rm vol} + \Delta_{\mathbf{k}d}^{\rm struc} , \tag{21}$$

where $E_d^{\rm struc}$ and $\Delta_{\mathbf{k}d}^{\rm struc}$ are small structural components associated with overlapping potentials from neighboring sites in the solid. Solution of the Schrödinger equation (7) subject to the constraints (14)–(17) then effectively completes the zeroth-order pseudoatom construction and provides all of the basic ingredients needed to treat the solid.

The remaining task is to develop the series (1) in terms of the weak matrix elements $W_{\mathbf{k}\mathbf{k}'}$, $S_{dd'}$, $\Delta_{dd'}$, $S_{\mathbf{k}d}$, and $\Delta_{\mathbf{k}d}$ and related quantities. This requires the introduction of Green's functions and an intricate analysis in which the volume and structural components of all terms are carefully separated, as in Eqs. (20) and (21). The central results obtained in Ref. 10 that are of direct interest here are as follows. The total electron density in the solid can be written in the form

$$n(\mathbf{r}) = n_{\rm val}(\mathbf{r}) + \sum_i n_{\rm core}(\mathbf{r} - \mathbf{R}_i) , \tag{22}$$

where $n_{\rm core}$ is the localized inner-core plus occupied valence d-state density

$$n_{\rm core}(\mathbf{r}) = 2\sum_c \langle \mathbf{r}|\phi_c\rangle\langle\phi_c|\mathbf{r}\rangle + (Z_d/5)\sum_d \langle \mathbf{r}|\phi_d\rangle\langle\phi_d|\mathbf{r}\rangle , \tag{23}$$

and $n_{\rm val}$ includes all remaining valence-electron density corresponding to Z electrons per atom. The latter is then primarily s and p in character and more or less uniform outside the inner-core regions. Similarly, the total energy of the solid can be partitioned into valence-binding, core, and valence-core-overlap contributions:

$$E_{\rm tot} = N(E_{\rm bind} + E_{\rm core} + E_{\rm val\text{-}core}) , \tag{24}$$

where the core energy $E_{\rm core}$ and the valence-core-overlap energy $E_{\rm val\text{-}core}$ are atomiclike quantities. The remaining valence-binding energy $E_{\rm bind}$ can then be obtained in terms of the effective valence-band-structure energy

$$E_{\rm band}^{\rm val} \equiv 2\sum_\alpha E_\alpha - NZ_d E_d , \tag{25}$$

where the sum is over all occupied valence energy levels. From Eq. (28) of Ref. 10, one obtains (apart from a zero-of-energy constant discussed in Appendix A)

$$E_{\rm bind} = \frac{1}{N}\left[\tfrac{1}{2}{\sum_{i,j}}' \frac{(Ze)^2}{|\mathbf{R}_i - \mathbf{R}_j|} + E_{\rm band}^{\rm val} - \tfrac{1}{2} n_{\rm val} V_{\rm val} + n_{\rm val}[\varepsilon_{\rm xc}(n_{\rm val}) - \mu_{\rm xc}(n_{\rm val})] \right.$$
$$+ \tfrac{1}{2}{\sum_{i,j}}' \left[\frac{(Z_a - Z)^2 e^2}{|\mathbf{R}_i - \mathbf{R}_j|} - 2n_i \frac{(Z_a - Z)e^2}{|\mathbf{r} - \mathbf{R}_j|} + n_i v_j \right] + {\sum_{i,j}}' \left[\frac{(Z_a - Z)Ze^2}{|\mathbf{R}_i - \mathbf{R}_j|} - n_i \frac{Ze^2}{|\mathbf{r} - \mathbf{R}_j|} \right]$$
$$\left. + \tfrac{1}{2}{\sum_{i,j}}' [n_i \mu_{\rm xc}^*(n_j) + \delta\varepsilon_{\rm xc}^*(n_i, n_j) - n_{\rm val}\,\delta\mu_{\rm xc}^*(n_i, n_j)] \right] , \tag{26}$$

where $n_i \equiv n_{\rm core}(\mathbf{r} - \mathbf{R}_i)$, $v_j \equiv v_{\rm core}(\mathbf{r} - \mathbf{R}_j)$, and an integration over volume is implied in all terms involving $n_{\rm val}$ and n_i, with $V_{\rm val}$ and v_j the Coulomb potentials arising from $n_{\rm val}$ and n_j, respectively. The terms on the first line of Eq. (26) are the same as those in the local-density total energy of a system with electron density $n_{\rm val}$ in an external field of the nuclei and $n_{\rm core}$, except that here the valence-band-structure energy $E_{\rm band}^{\rm val}$ contains a large ex-

tra contribution to the cohesion from the d electrons. The two groups of terms on the second line of Eq. (26) represent the exact Coulomb corrections due to overlapping electron densities n_i, while the final group of terms on the third line represents the corresponding contribution from exchange and correlation. The latter arises from systematic expansions of exchange-correlation potential $\mu_{xc}(n)$ and energy $\varepsilon_{xc}(n)$ in terms of the same overlapping densities, neglecting only three-ion and higher overlap contributions. These expansions are developed in terms of the *localized* exchange-correlation functions

$$\mu^*_{xc}(n_i)\equiv\mu_{xc}(n_i+n_{val})-\mu_{xc}(n_{val}) \tag{27}$$

and

$$\varepsilon^*_{xc}(n_i)\equiv\varepsilon_{xc}(n_i+n_{val})-\varepsilon_{xc}(n_{val}) , \tag{28}$$

with the precise definitions of $\delta\mu^*_{xc}$ and $\delta\varepsilon^*_{xc}$ in terms of these quantities given by Eqs. (11) and (15) of Ref. 10, respectively. Note that since the Coulomb and exchange-correlation corrections in Eq. (26) consist of pairwise additive terms, they will contribute directly to the total two-ion pair potential v_2 in Eq. (1).

One additional ingredient must be included to cancel core and valence-core-overlap energies between the solid and the free atom and obtain the cohesive energy in terms of valence binding energies. In the usual case, Z and Z_d in the solid will differ from their corresponding values in the free atom, say Z^0 and Z^0_d. To achieve the desired cancellations, one must first transfer the required number of s and d electrons in the free atom to match Z and Z_d. This costs an atomic preparation energy, E_{prep}, which can be readily calculated within density-functional theory, as also discussed in Ref. 10. Then the cohesive energy is just

$$\begin{aligned}E_{coh}&\equiv\frac{1}{N}E^{solid}_{tot}(Z)-E^{atom}_{tot}(Z^0)\\&=E^{solid}_{bind}(Z)-E^{atom}_{bind}(Z)+E_{prep} ,\end{aligned} \tag{29}$$

where E^{solid}_{bind} is to be calculated from Eq. (26) and E^{atom}_{bind} is the corresponding binding energy of a free atom with Z valence s electrons and Z_d valence d electrons. The last two terms on the second line of Eq. (29) are now volume dependent in general (because Z and Z_d are volume dependent) and hence contribute to the volume term E_{vol} in the cohesive energy functional[12]

$$\begin{aligned}E_{coh}(\mathbf{R}_1,\ldots,\mathbf{R}_N)=E_{vol}(\Omega)&+\frac{1}{2N}{\sum_{i,j}}' v_2(i,j)\\&+\frac{1}{6N}{\sum_{i,j,k}}' v_3(i,j,k)\\&+\frac{1}{24N}{\sum_{i,j,k,l}}' v_4(i,j,k,l)+\cdots ,\end{aligned} \tag{30}$$

while the remaining interatomic potentials v_2, v_3, and v_4 are now to be derived entirely from Eq. (26).

Finally, to obtain theoretical expressions for E_{vol}, v_2, v_3, and v_4, one must evaluate Eq. (25) for the valence-band-structure energy E^{val}_{band}. This can be done in terms of components of the *integrated* density of one-electron states, $N(E)$. Writing

$$N(E)=N_0(E)+N_d(E)+\delta N_{sp}(E)+\delta N_d(E) , \tag{31}$$

where N_0 and N_d are the free-electron and one-ion d-resonance components and δN_{sp} and δN_d are the small oscillatory structural components due to the s and p electrons and the d electrons, respectively, one can derive the exact result

$$\begin{aligned}E^{val}_{band}=\tfrac{3}{5}NZ\varepsilon_F+NE^d_{vol}&-\int_0^{\varepsilon_F}\delta N_{sp}(E)dE\\&-\int_0^{\varepsilon_F}\delta N_d(E)dE-NZ_dE^{struc}_d+\delta E_{band} .\end{aligned} \tag{32}$$

Here, E^d_{vol} is the one-ion d-state component to E_{vol},

$$\begin{aligned}E^d_{vol}&\equiv\frac{1}{N}\int_0^{\varepsilon_F}(E-E^{vol}_d)\rho_d(E)dE\\&=Z_d(\varepsilon_F-E^{vol}_d)-(10/\pi)\int_0^{\varepsilon_F}\delta_2(E)dE ,\end{aligned} \tag{33}$$

with $\rho_d=dN_d/dE$ the one-ion d-state density of states, and δE_{band} is a correction term involving the true Fermi energy. The fact that the d-band width is proportional to the d-resonance width associated with the phase shift δ_2 is sufficient to ensure that the increased cohesion in transition metals over simple metals is already largely contained in E^d_{vol}. Moreover, the zeroth-order pseudoatom cohesive energy

$$E^{pa}_{coh}\equiv\tfrac{3}{5}Z\varepsilon_F+E^d_{vol}+\frac{2\Omega}{(2\pi)^3}\int_{k<k_F}\langle\mathbf{k}|w'_{pa}|\mathbf{k}\rangle d\mathbf{k}+Z\varepsilon_{xc}(n_{unif})-\tfrac{3}{5}(Ze)^2/R_{WS}-E^{atom}_{bind}(Z)+E_{prep} , \tag{34}$$

which explicitly contains the first two terms in Eq. (32) and is the leading contribution to E_{vol} in Eq. (30), already well approximates the cohesive energy of the actual metal. In all of the $3d$ and $4d$ transition metals, E^{pa}_{coh} agrees to within 20% with self-consistent band-structure calculations of the cohesive energy. In Eq. (34), w'_{pa} is an appropriate one-site component of the pseudopotential W, as discussed in Appendix A.

The major additional contributions to the interatomic potentials v_2, v_3, and v_4 come from the integrals over δN_{sp} and δN_d in Eq. (32). The former integral is developed in powers of the pseudopotential W and to second order yields familiar simple-metal-like contributions to v_2. The latter integral, on the other hand, is developed in powers of the dimensionless d-state coupling strength

$$t^{vol}_{dd'}(R_{ij},E)\equiv\frac{(E-E^{vol}_d)S_{dd'}(R_{ij})+\Delta^{vol}_{dd'}(R_{ij})-\Gamma^{vol}_{dd'}(R_{ij},E)}{E-E^{vol}_d-\Gamma^{vol}_{dd}(E)} \tag{35}$$

between sites i and j at energy E, where the quantity $\Gamma_{dd'}^{\rm vol}(R_{ij},E)$ is a long-range hybridization interaction term which reduces to $\Gamma_{dd}^{\rm vol}(E)$ for $d=d'$ and $R_{ij}=0$. This gives rise to a series of d-state potentials:

$$v_2^d(i,j)=-\frac{2}{\pi}\mathrm{Im}\int_0^{\epsilon_F}\mathrm{Tr}[T_{ij}T_{ji}+\tfrac{1}{2}(T_{ij}T_{ji})^2+\cdots]dE\ , \tag{36}$$

$$v_3^d(i,j,k)=-\frac{2}{\pi}\mathrm{Im}\int_0^{\epsilon_F}\mathrm{Tr}[-2(T_{ij}T_{jk}T_{kl})+(T_{ij}T_{ji}T_{jk}T_{kj}+T_{jk}T_{kj}T_{ki}T_{ik}+T_{ki}T_{ik}T_{ij}T_{jl})+\cdots]dE\ , \tag{37}$$

and

$$v_4^d(i,j,k,l)=-\frac{2}{\pi}\mathrm{Im}\int_0^{\epsilon_F}\mathrm{Tr}[2(T_{ij}T_{jk}T_{kl}T_{li}+T_{ik}T_{kl}T_{lj}T_{ji}+T_{il}T_{lj}T_{jk}T_{ki})+\cdots]dE\ . \tag{38}$$

Here, T_{ij} is the 5×5 matrix made up of components $t_{dd'}^{\rm vol}(R_{ij},E)$ and Tr denotes the trace of the matrix product in square brackets. The higher-order terms in Eqs. (36)–(38) may actually be summed in each case to include all multiple-scattering-like contributions to the potentials, as described in Ref. 10, with the complete expressions given by Eqs. (97)–(104) of that paper. The asymptotic forms (36)–(38) are valid to fourth order in $t_{dd'}^{\rm vol}$. In tight-binding language, it may be said that Eqs. (36)–(38) include all band-structure contributions through the fourth moment of the total d-band density of states.

The full two-ion pair potential has the form

$$v_2(r)=\frac{(Z^*e)^2}{r}\left[1-\frac{2}{\pi}\int_0^{\infty}F_N^0(q)\frac{\sin(qr)}{q}dq\right]+v_2^d(r)+v_{\rm ol}^0(r)\ . \tag{39}$$

Here the first term is a screened Coulomb interaction which depends on an effective valence Z^* and a normalized energy–wave-number characteristic F_N^0. The quantities Z^* and F_N^0 are functionals of pseudopotential and hybridization matrix elements, with the complete expressions given by Eqs. (133) and (134) and Eqs. (136) and (140), respectively, of Ref. 10. The third term in Eq. (39) is a short-range overlap potential which includes the electrostatic and exchange-correlation contributions from the second and third lines of Eq. (26) for the binding energy of the solid. The complete expression for $v_{\rm ol}^0$ is given by Eq. (137) of Ref. 10. The multi-ion potentials v_3 and v_4, on the other hand, are dominated by their d-state band-structure contributions, so that one takes $v_3=v_3^d$ and $v_4=v_4^d$.

III. MODEL GPT FOR CENTRAL TRANSITION METALS

A. Analytic d-state potentials

The model GPT is developed within exactly the same framework as the first-principles theory, but with the introduction of additional simplifying approximations. The simplifications begin with an ansatz: we neglect the troublesome long-range oscillatory tails of the potentials v_2, v_3, and v_3. In transition metals, these tails arise primarily through indirect hybridization interactions contained in $F_N^0(q)$ and $\Gamma_{dd'}^{\rm vol}(R_{ij},E)$, which couple d states on different sites. It has been found from the first-principles GPT, however, that these hybridization tails destructively interfere in the calculation of materials properties when the d bands are partially occupied. Physically, this destructive interference is a consequence of the nonspherical nature of the Fermi surface in such transition metals which tends to inhibit any net long-range hybridization interaction between ions. Clearly, the destructive interference is most complete for the central transition metals (e.g., V, Nb, Cr, and Mo), so that the model GPT is focused primarily on this subset of materials.

Next, we simplify the description of the remaining direct d-d couplings between ions. As may be done in the first-principles GPT, the two-ion d-state nonorthogonality contributions arising from terms involving $S_{dd'}$ which remain nonzero as $Z_d\to10$ are first subtracted from v_2^d and then added back to $v_{\rm ol}^0$ to form a repulsive hard-core-like potential $v_2^{\rm hc}$. All remaining two-, three-, and four-ion contributions involving $S_{dd'}$ are now dropped in the model GPT, however, so that Eq. (35) for $t_{dd'}^{\rm vol}$ is effectively reduced to

$$t_{dd'}^{\rm vol}(R_{ij},E)=\frac{\Delta_{dd'}^{\rm vol}(R_{ij})}{E-E_d^{\rm vol}-\Gamma_{dd}^{\rm vol}(E)}\ . \tag{40}$$

We then introduce canonical d bands to express the remaining $\Delta_{dd'}^{\rm vol}$ matrix elements analytically and retain direct couplings to only fourth order, so that Eqs. (36)–(38) apply. The d-state band-structure contributions to the interatomic potentials can also be expressed diagramatically in this case, and the relevant diagrams contributing to v_2, v_3, and v_4 are illustrated in Fig. 1. Here each line in a diagram connecting two ion sites represents a 5×5 matrix made up of elements $\Delta_{dd'}^{\rm vol}$ (or $t_{dd'}^{\rm vol}$), while the cohesive energy contribution corresponding to a complete diagram is proportional to the trace of the resulting matrix product. In a pure canonical d-band description,[13–15]

$$\Delta_{dd'}^{\rm vol}(R_{ij})=\alpha_m(R_{\rm WS}/R_{ij})^5\ , \tag{41}$$

where $5=2l+1$ for $l=2$ and $R_{\rm WS}$ is the Wigner-Seitz radius. Here the α_m are structure-independent coefficients with fixed ratios between the m components such that $\alpha_0{:}\alpha_1{:}\alpha_2$ is $6{:}(-4){:}1$. Utilizing such a description of $\Delta_{dd'}^{\rm vol}$ permits all of the diagrams to be evaluated analytically. In practice, one can obtain a somewhat more accurate description of the $\Delta_{dd'}^{\rm vol}$ matrix elements for real metals, without losing the analytic nature of the canonical

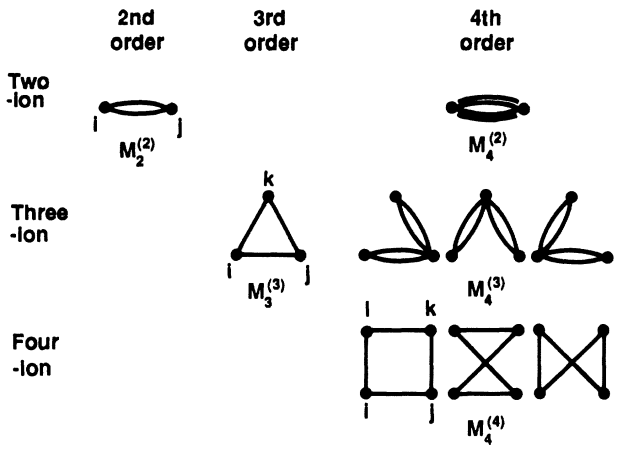

FIG. 1. Graphical representation of the d-state band-structure contributions to the interatomic potentials v_2^d, v_3^d, and v_4^d, with the notation as in Ref. 10.

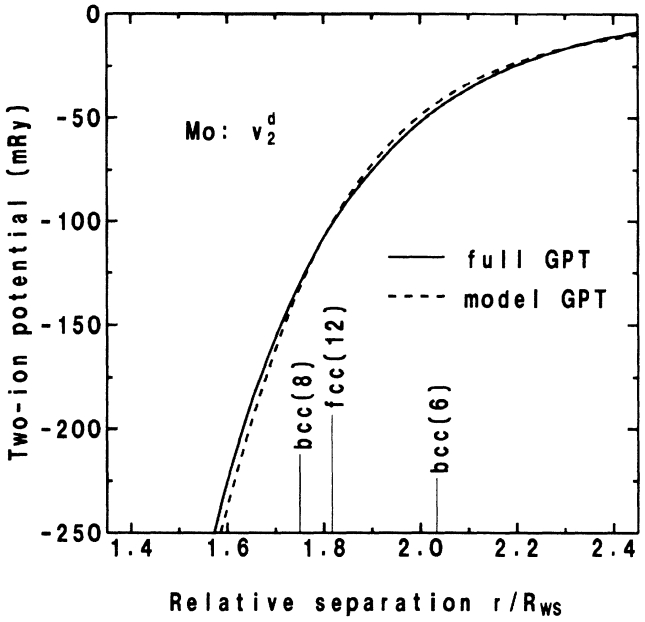

FIG. 2. Two-ion d-state potential v_2^d for Mo, as calculated from the model GPT with $p=4$ in Eq. (43) and from the full first-principles GPT via Eq. (36), but neglecting the sp-d hybridization contributions from $\Gamma_{dd'}^{\rm vol}(R_{ij},E)$. The position and number of bcc and fcc near neighbors is indicated.

description, by generalizing the R_{ij} dependence of Eq. (41) to

$$\Delta_{dd'}^{\rm vol}(R_{ij})=\alpha_m(R_{\rm WS}/R_{ij})^p\ , \tag{42}$$

where p is a material-dependent constant.

The two-ion d-state potential v_2^d in the model GPT consists of one second-order and one fourth-order contribution. Using Eqs. (40) and (42) in Eq. (36), one is immediately led to a general form

$$\begin{aligned} v_2^d(r)&=v_a[f(r)]^4-v_b[f(r)]^2 \\ &=v_a(r_0/r)^{4p}-v_b(r_0/r)^{2p}\ , \end{aligned} \tag{43}$$

where

$$f(r)\equiv(r_0/r)^p \tag{44}$$

is a characteristic radial function, with $r_0\equiv 1.8R_{\rm WS}$. The quantities v_a and v_b are material-related parameters which depend primarily on d-band filling and width, and may be analyzed separately, as discussed in Sec. III B below. From general theoretical considerations, one expects that for the central transition metals $v_a>0$ and $v_b>0$ with $v_b\gg v_a$, so that v_2^d is an entirely attractive potential in the physical region of interest. With $p=5$ in Eq. (43), one has the canonical d-band result

$$v_2^d(r)=v_a(r_0/r)^{20}-v_b(r_0/r)^{10}\ . \tag{45}$$

For the representative case of Mo, on the other hand, the choice $p=4$ in Eq. (43) leads to a near-optimum fit to the corresponding first-principles GPT calculation of v_2^d when v_a and v_b are treated as free parameters, as shown in Fig. 2.

As an aside, it is interesting and instructive to note the corresponding form of canonical p- and f-band two-ion potentials. That is, the above analysis can be applied to energy bands of any angular momentum l with the general result that the second-order attractive component of v_2^l varies as $r^{-2(2l+1)}$ while the repulsive fourth-order component varies as $r^{-4(2l+1)}$. Thus for p states with $l=1$, one has

$$v_2^p(r)=v_a(r_0/r)^{12}-v_b(r_0/r)^6\ , \tag{46}$$

which is of the same form as the classic Lennard-Jones potential normally assumed for rare-gas solids.[16] In metals, such p-band potentials have possible relevance to the second-period elements Li and Be with strong p-state interactions. For the case of f states with $l=3$, on the other hand, one obtains

$$v_2^f(r)=v_a(r_0/r)^{28}-v_b(r_0/r)^{14}\ , \tag{47}$$

which has direct application to the actinide metals.[17]

Returning to the case of transition metals, the two-ion d-state potential v_2^d must be combined with the hard-core contribution $v_2^{\rm hc}$ and a simple-metal-like screened Coulomb contribution for the s and p electrons, v_2^{sp}. The latter is of the same form as the first term in Eq. (39) with Z^* and F_N^0 evaluated in the limit of no sp-d hybridization. Then the total two-ion pair potential is

$$v_2(r)=v_2^{sp}(r)+v_2^{\rm hc}(r)+v_2^d(r)\ . \tag{48}$$

Since both v_2^{sp} and $v_2^{\rm hc}$ are readily calculable from the first-principles theory, these quantities are retained without change in the model GPT. In Fig. 3, v_2 and its components are illustrated for the case of Mo, with v_2^d obtained from Eq. (43) in the same manner as in Fig. 2.

The three-ion triplet potential is dominated by d-state band-structure contributions, so that we always take $v_3=v_3^d$, as is done in the first-principles GPT. From either Eq. (37) or Fig. 1, it can be seen that there are one third-order and three fourth-order contributions to v_3^d, leading via Eqs. (40) and (42) to a general form

$$v_3(r_1,r_2,r_3)=v_c f(r_1)f(r_2)f(r_3)L(\theta_1,\theta_2,\theta_3)+v_d\{[f(r_1)f(r_2)]^2P(\theta_3)+[f(r_2)f(r_3)]^2P(\theta_1)+[f(r_3)f(r_1)]^2P(\theta_2)\}\ , \tag{49}$$

where θ_1, θ_2, and θ_3 are the angles subtended by r_1, r_2, and r_3, respectively, as indicated in Fig. 4(a). Here, L is the angular function

$$L(\theta_1,\theta_2,\theta_3)\equiv L(x_1,x_2,x_3)=\tfrac{1}{144}[54+330x_1x_2x_3-105(x_1^2x_2^2+x_2^2x_3^2+x_3^2x_1^2)+735(x_1x_2x_3)^2]\ , \tag{50}$$

with $x_1\equiv\cos\theta_1$, $x_2\equiv\cos\theta_2$, and $x_3\equiv\cos\theta_3$, and P is the additional angular function

$$P(\theta)\equiv P(x)=\tfrac{1}{1448}(533+510x^2+405x^4)\ , \tag{51}$$

with $x\equiv\cos\theta$. Both L and P are universal functions which depend only on d symmetry and apply to all transition metals; their behavior is illustrated in Fig. 4(b). Equations (50) and (51) are obtained directly from the analytic matrix multiplication of the $\Delta_{dd'}^{\rm vol}$ with $\alpha_0{:}\alpha_1{:}\alpha_2$ fixed at $6{:}(-4){:}1$, as described in Appendix B. It can be further shown[17] that the third-order term in Eq. (49) involving L is the exact d-state analog of the classic Axilrod-Teller potential,[18] which one obtains for the case of p states. More generally, the radial and angular functions for canonical p bands all exhibit dipole symmetry, while those for canonical d bands all exhibit quadrupole symmetry.

The coefficients v_c and v_d in Eq. (49) are additional material-dependent parameters that again mostly reflect d-band filling and width. For almost half-filled d bands, v_c is near zero while v_d is positive, so that $v_d>|v_c|$ and v_3 is an entirely repulsive potential, as is shown in Fig. 5 for Mo. As in the case of v_2^d, it is seen that the model GPT can provide a rather good fit to the first-principles theory with v_c and v_d treated as free parameters and utilizing a choice $p=4$ in Eq. (44) for $f(r)$.

Similarly, for the four-ion quadruplet potential we take $v_4=v_4^d$. From Eq. (39) or Fig. 1, it can be seen that there are three fourth-order contributions to v_4^d, so that one has a form

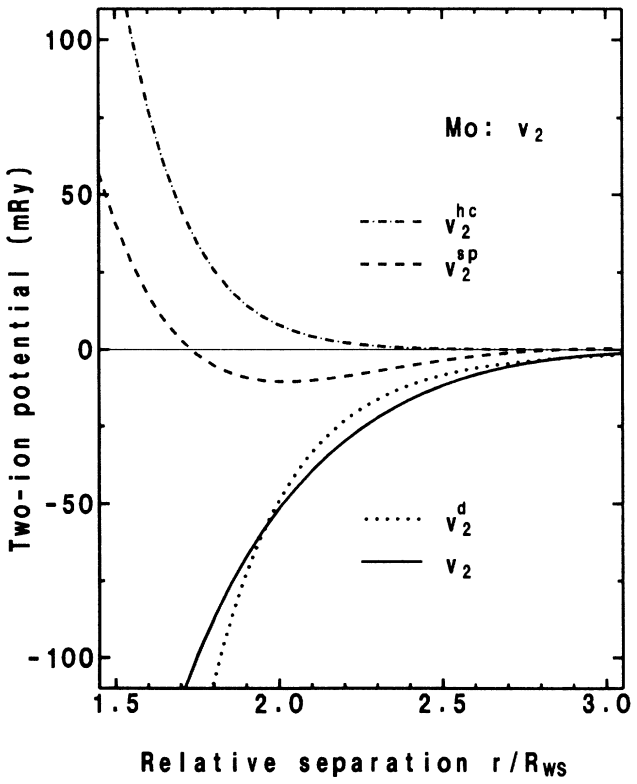

FIG. 3. Full two-ion potential v_2 and its simple-metal, hard-core, and d-state components, v_2^{sp}, v_2^{hc}, and v_2^d, respectively, for Mo.

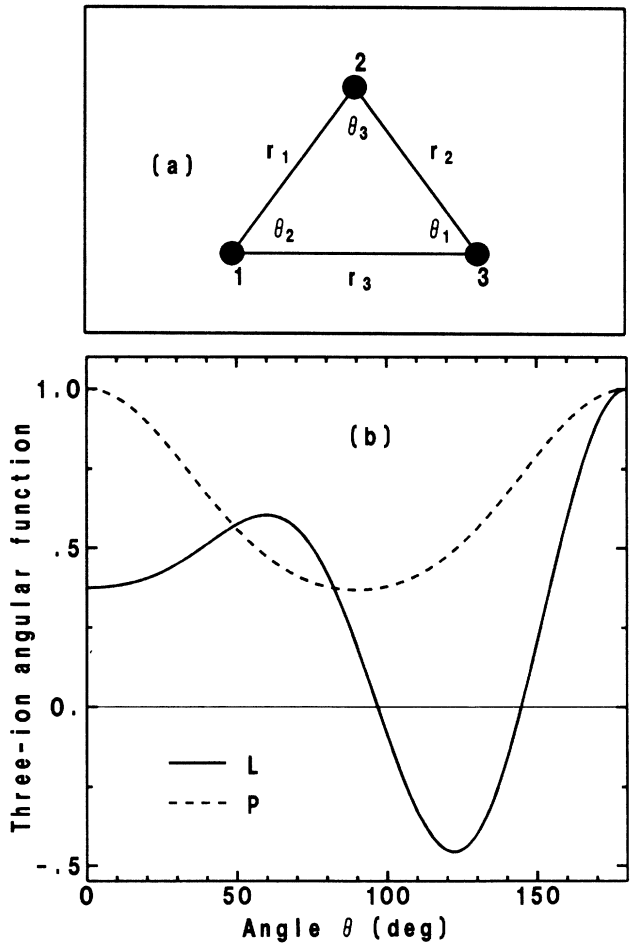

FIG. 4. (a) Three distances and angles defined for general three-ion interactions. (b) Three-ion angular functions L and P, as given by Eqs. (50) and (51), with $\theta\equiv\theta_3$ and $\theta_1=\theta_2=(\pi-\theta)/2$.

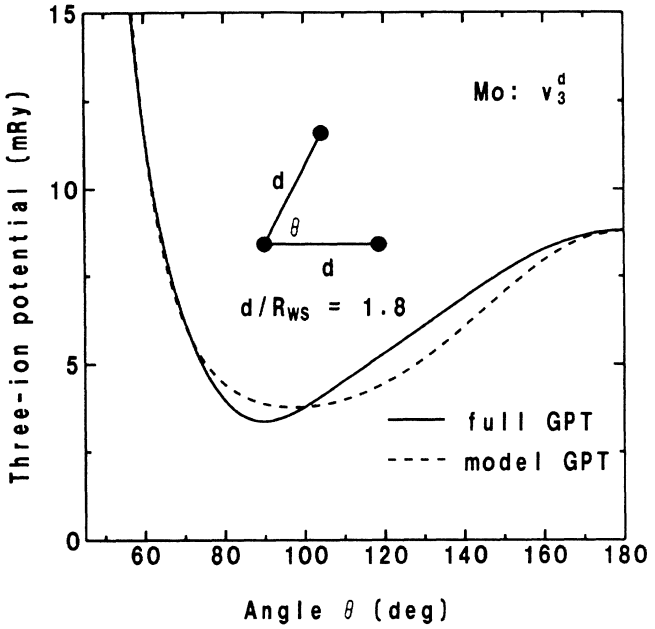

FIG. 5. Three-ion potential $v_3=v_3^d$ in Mo for the special case $r_1=r_2=1.8R_{\rm WS}$, as calculated from the model GPT with $p=4$ in Eq. (49) and from the full first-principles GPT via Eq. (37), but neglecting the *sp-d* hybridization contributions from $\Gamma_{dd'}^{\rm vol}(R_{ij},E)$.

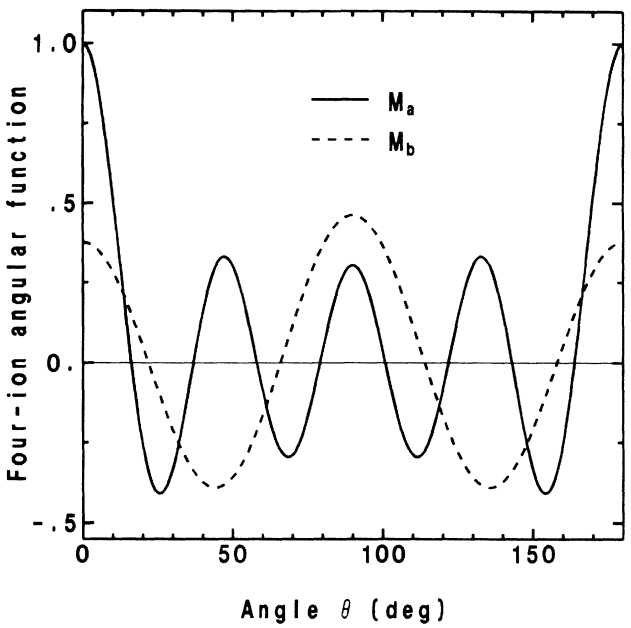

FIG. 7. Four-ion angular functions $M_a(\theta)$ and $M_b(\theta/2)$ for coplanar interactions, as given by Eqs. (53) and (54).

$$v_4(r_1,r_2,r_3,r_4,r_5,r_6)=v_e[f(r_1)f(r_2)f(r_4)f(r_5)M(\theta_1,\theta_2,\theta_3,\theta_4,\theta_5,\theta_6)+f(r_3)f(r_2)f(r_6)f(r_5)M(\theta_7,\theta_8,\theta_9,\theta_{10},\theta_5,\theta_{12})$$
$$+f(r_1)f(r_6)f(r_4)f(r_3)M(\theta_{11},\theta_{12},\theta_5,\theta_6,\theta_3,\theta_4)]\ , \tag{52}$$

where M is a third universal angular function which depends only on d symmetry, and v_e is an additional material-dependent parameter. The function M has also been obtained analytically, but with six independent variables its general form is rather more complicated than L or P. The full analytic result is given in Appendix B, while the precise definitions of the six distances $r_1,\ldots,r_6$ and 12 angles $\theta_1,\ldots,\theta_{12}$ associated with four-ion geometry are given in Fig. 6. For the special case of coplanar interactions with $r_1=r_2=r_4=r_5$, M can be expressed in terms of a single angle θ as $M(\theta)\equiv M(x)$ with $x=\cos\theta$. For configuration (a) in Fig. 6 with $\theta=\theta_1=\theta_3$ or $\theta=\theta_2=\theta_4$,

$$M_a(x)=\tfrac{1}{5792}(1757-60\,460x^2+327\,870x^4$$
$$-563\,500x^6+300\,125x^8)\ , \tag{53}$$

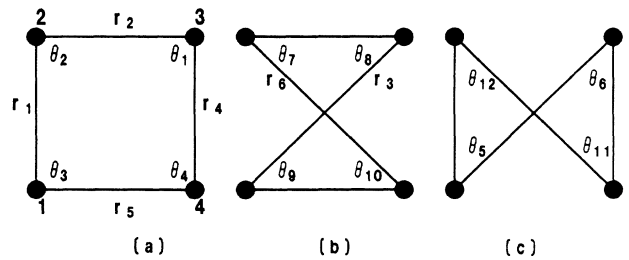

FIG. 6. Six distances and 12 angles defined for the general four-ion interactions corresponding to configurations (a)–(c).

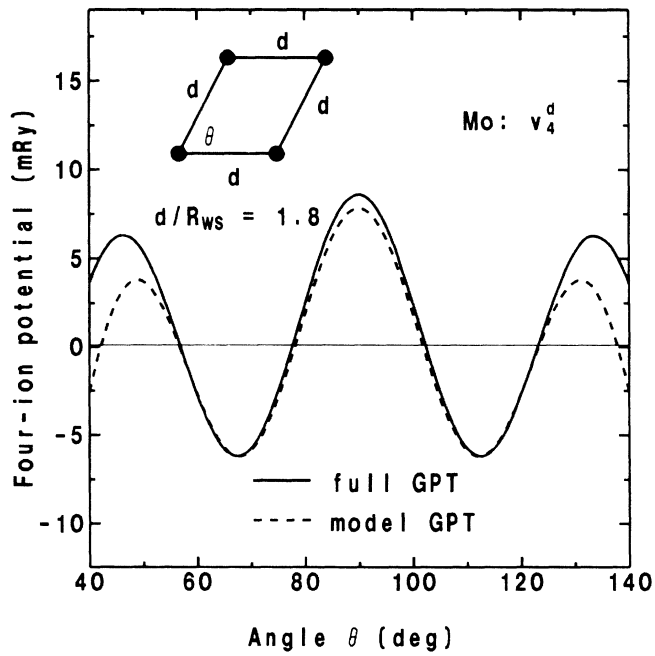

FIG. 8. Four-ion potential $v_4=v_4^d$ in Mo for the special case of coplanar interactions with $r_1=r_2=r_4=r_5=1.8R_{\rm WS}$, as calculated from the model GPT with $p=4$ in Eq. (52) and from the full first-principles GPT via Eq. (38), but neglecting the *sp-d* hybridization contributions from $\Gamma_{dd'}^{\rm vol}(R_{ij},E)$.

while for configuration (b) with $\theta=\theta_7=\theta_{10}$ or $\theta=\theta_8=\theta_9$ [or for configuration (c) with $\theta=\theta_5=\theta_6$ or $\theta=\theta_{11}=\theta_{12}$],

$$M_b(x)=\tfrac{1}{5792}(2172-73\,020x^2+373\,145x^4 -600\,250x^6+300\,125x^8) . \quad (54)$$

The behavior of M_a and M_b is illustrated in Fig. 7. Unlike v_2 and v_3, the sinusoidal nature of M makes v_4 oscillatory in sign. Again the model GPT, with $p=4$ and v_e treated as a free parameter, well reproduces the structure of the corresponding first-principles potential, as shown in Fig. 8 for Mo. While v_4 necessarily leads to a much smaller cohesive-energy contribution than either v_2 or v_3, it is important to many structural properties connected with bcc stability. This can be inferred from Fig. 8, where it can be seen that v_4 is minimum near the prominent 70.5° angle contained in the bcc structure and maximum at the prominent 90° angle contained in the fcc structure.

B. Nature of the *d*-state-potential coefficients

The material-dependent parameters v_a, v_b, v_c, v_d, and v_e in the model GPT can be determined either by (i) direct evaluation, at some level of approximation, or (ii) by imposing a limited number of theoretical constraints and then selectively fitting to the first-principles potentials, to calculated first-principles physical properties, and/or to experimental data. Procedure (i) allows one to understand, in qualitative terms, the general nature of the *d*-state-potential coefficients and their interrelationships, and we follow this course in the present subsection. Procedure (ii), on the other hand, allows one to optimize the theory by effectively minimizing the quantitative error in the model GPT for real materials. We have developed a number of different schemes to carry out the latter, but we defer discussion of these until Sec. IV, where the model GPT is applied to an accurate description of the physical properties of Mo.

To proceed with an approximate evaluation of the *d*-state potential parameters, we first define

$$\Gamma_0\equiv-\mathrm{Im}[\Gamma_{dd}^{\mathrm{vol}}(\varepsilon_F)] \quad (55)$$

and

$$E_0\equiv E_d^{\mathrm{vol}}+\mathrm{Re}[\Gamma_{dd}^{\mathrm{vol}}(\varepsilon_F)] . \quad (56)$$

Then Γ_0 is a positive quantity on the order of one-half of the *d*-band width and E_0 is an energy near the center of the *d* band. Using Eqs. (14) and (17), one can express the *d*-band occupation number Z_d exactly in terms of these quantities:

$$Z_d=(10/\pi)\tan^{-1}[\Gamma_0/(E_0-\varepsilon_F)]$$

or (57)

$$(\varepsilon_F-E_0)/\Gamma_0=-\cot(\pi Z_d/10) .$$

The dependence of the *d*-state-potential coefficients on Z_d is contained in the normalized integrals

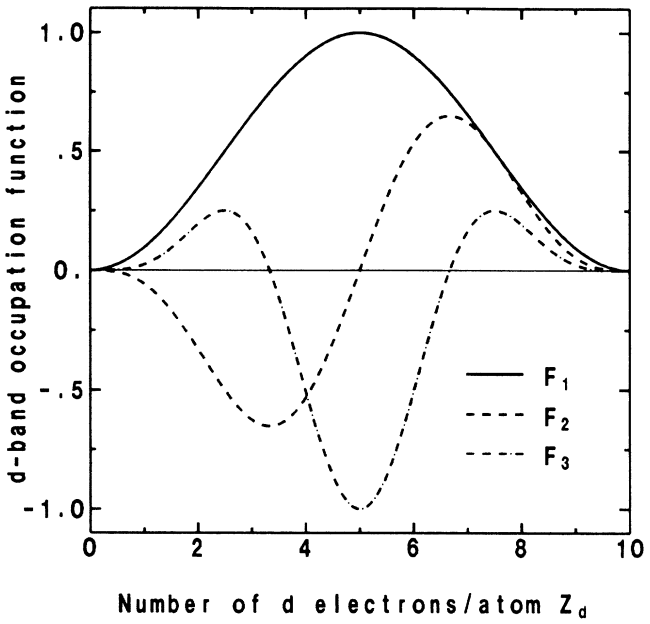

FIG. 9. The *d*-state occupation functions $F_n(Z_d)$ as given by Eq. (59) for $n=1$, 2, and 3.

$$F_n(Z_d)\equiv\mathrm{Im}\int_0^{\varepsilon_F}\frac{n(\Gamma_0)^n}{[E-E_d^{\mathrm{vol}}-\Gamma_d^{\mathrm{vol}}(E)]^{n+1}}dE . \quad (58)$$

With $t_{dd'}^{\mathrm{vol}}$ approximated by Eq. (40), each of the energy integrals in Eqs. (36)–(38) is proportional to F_n for $n=1$, 2, or 3. The right-hand side of Eq. (58) can be evaluated analytically without losing any important feature of the result, if one neglects the energy dependence of $\Gamma_{dd}^{\mathrm{vol}}$ and extends the lower limit to $-\infty$. Using Eqs. (55)–(57), one thereby obtains

$$F_n(Z_d)=-\mathrm{Im}\{[-\cot(\pi Z_d/10)+i]^{-n}\} . \quad (59)$$

The F_n are thus simple oscillatory functions of Z_d bounded by the condition $-1\le F_n\le 1$. The specific results for $n=1$, 2, and 3 are plotted in Fig. 9.

The final ingredients needed to complete the analysis are explicit forms for the coefficients α_m in the *d*-state matrix elements $\Delta_{dd'}^{\mathrm{vol}}$, as defined by Eq. (41) for canonical *d* bands. Here we exploit the fact that $\Delta_{dd'}^{\mathrm{vol}}$ and Γ_0 can both be expressed approximately in terms of the same *intra*-atomic matrix element,[19] so that α_m and Γ_0 are proportional. From Eq. (118) of Ref. 10, one finds

$$\alpha_m=\eta_m C_Z\Gamma_0 , \quad (60)$$

where $\eta_m=6$, -4, or 1 for $m=0$, ±1, or ±2, and where

$$C_Z\equiv\frac{45}{(9\pi Z/4)^{5/3}} . \quad (61)$$

It is then entirely straightforward to evaluate the *d*-state-potential coefficients from Eqs. (36)–(38). One obtains

$$v_b=v_b^0C_Z^2F_1(Z_d)\Gamma_0 , \quad (62)$$

with $v_b^0\equiv(140/\pi)(1.8)^{-10}=0.124\,81$;

$$v_c=v_c^0C_Z^3F_2(Z_d)\Gamma_0 , \quad (63)$$

TABLE I. Ratios of d-state-potential coefficients obtained from the simplified model presented in the text, Eqs. (62)–(66), and from fitting first-principles GPT potentials for Mo. In the latter, the $p=4$ case corresponds to the results presented in Figs. 2, 5, 8, and 10 and in Table II. In all three cases, $Z=1.402$ and $Z_d=4.598$.

	Model ($p=5$)	Fit ($p=5$)	Fit ($p=4$)
v_a/v_d	0.5	1.213	1.122
v_b/v_d	46.40	13.32	13.42
v_c/v_d	−0.7765	−0.1933	−0.1937
v_e/v_d	2.0	2.419	2.448

with $v_c^0 \equiv (180/\pi)(1.8)^{-15} = 0.008\,492\,5$;

$$v_d = -v_d^0 C_Z^4 F_3(Z_d)\Gamma_0 , \tag{64}$$

with $v_d^0 \equiv (3620/3\pi)(1.8)^{-20} = 0.003\,012\,9$;

$$v_a = v_d/2 ; \tag{65}$$

and

$$v_e = 2v_d . \tag{66}$$

At normal density, the quantity C_Z is a constant on the order of unity; for $Z=1.4$, $C_Z=0.986\,53$. Then each coefficient is directly proportional to the d-band width and varies with d-band filling according to F_1, F_2, or F_3. Since $F_1 \geq 0$, Eq. (62) for the two-ion-potential coefficient v_b predicts $v_b \geq 0$ for all Z_d with a maximum value at $Z_d=5$ (half-filled d bands). The remaining four coefficients, on the other hand, are expected to oscillate in sign as a function of d-band filling. According to Eq. (63), the three-ion-potential coefficient v_c is negative for $Z_d<5$, vanishes at $Z_d=5$, and is positive for $Z_d>5$. From Eqs. (64)–(66), the coefficients v_a, v_d, and v_e are expected to be positive for $3.33 \leq Z_d \leq 6.67$ and maximum at $Z_d=5$, with v_a/v_d and v_e/v_d constant. In the case of Mo, the general behavior of the d-state-potential coefficients obtained from fitting the first-principles GPT potentials (Figs. 2, 5, and 8) are in qualitative accord with these results. Quantitatively, however, the model coefficients from Eqs. (62)–(66) differ substantially from the fitted coefficients regardless of the choice of the decay-law power p used in the fitting, as is shown in Table I. In particular, the model ratios v_b/v_d and $|v_c/v_d|$ are considerably larger than those obtained from the fitted coefficients. This reflects both the secondary approximations used in obtaining Eqs. (62)–(66) and the additional physics contained in the first-principles GPT.

C. Folding in higher-order contributions

Ultimately, the applicability of the model GPT to real materials is made possible because the theory correctly accounts for the *shapes*, as opposed to the *magnitudes*, of the first-principles potentials. Importantly, this remains true even when higher-order d-state contributions from $\Delta_{dd'}^{\rm vol}$ and $S_{dd'}$ to v_2^d, v_3^d, and v_4^d, beyond Eqs. (36)–(38), are taken into account. When the full expressions containing powers of $t_{dd'}^{\rm vol}$ to all orders, Eqs. (97)–(104) of Ref. 10, are used to evaluate the d-state potentials in the case of Mo, it is found that v_2^d is essentially unaffected while v_3^d and v_4^d for near-neighbor interactions are reduced in magnitude but remain substantially similar in shape. Thus, at short range, the effect of the higher-order terms can be formally absorbed into renormalized coefficients v_c, v_d, and v_e.

At the same time it must be noted that the same higher-order terms can lead to long-range interactions which have no counterpart in the model GPT. Graphically, the neglected higher-order terms correspond to all remaining possible graphs to the right in Fig. 1. Open-ended graphs consisting of chains of double lines connecting two ions can extend to arbitrarily long range even though the individual matrix elements $\Delta_{dd'}^{\rm vol}$ and $S_{dd'}$ remain short ranged. Such terms can contribute significantly to certain elastic-constant and phonon anomalies in the central transitions metals. In the group-VB elements (V, Nb, and Ta), for example, the pronounced softening of the transverse $T_2[110]$ phonons at long wavelengths and the corresponding small value of the C_{44} elastic constant are driven by such long-range d-state interactions.[11] In the group-VIB elements (Cr, Mo, and W), the same is true for the pronounced softening of the [100] phonons at the Brillouin-zone boundary.[10] Consequently, both of these effects are underestimated by the model GPT. This is the necessary price one must pay for a simplified description of the material in terms of short-range potentials.

At the other extreme, it is also of interest to consider to what extent the present three- and four-ion potentials, Eqs. (49) and (52), can be folded down into an effective pair potential to obtain the simplest possible description of the metal. Formally, such an effective pair potential can be obtained by averaging over the multi-ion potentials:

$$v_2^{\rm eff} = v_2 + \langle v_3 \rangle + \langle v_4 \rangle + \cdots . \tag{67}$$

The oscillatory nature of v_4 (and also higher-order potentials) will make its explicit contribution to $v_2^{\rm eff}$ negligibly small. For the case of nearly-half-filled d-band metals such as Mo, one can also neglect the three-ion contribution involving v_c. The remaining contributions from $\langle v_3 \rangle$ will produce terms proportional to $f^2(r)$, as already appear in v_2, so that one expects a form

$$v_2^{\rm eff}(r) = v_2^{sp}(r) + v_2^{\rm hc}(r) + v_a^*(r_0/r)^{4p} - v_b^*(r_0/r)^{2p} , \tag{68}$$

where $v_a^* \simeq v_a$, but $|v_b^*| \ll |v_b|$ since the repulsive nature of v_3 has now been folded back into v_b^*. In Table II we contrast the performance of $v_2^{\rm eff}$ as given by Eq. (68) with that of the multi-ion potentials v_2, v_3, and v_4 for Mo, using two free parameters (either v_a^* and v_b^* or v_b and v_d) fitted to cohesive properties in each case and then calculating some basic mechanical, structural, and vibrational properties which can be compared with experimental data.[20–26] It is seen there that even in the best circumstance the effective-pair-potential scheme can only describe average properties, such as $E_{\rm coh}$, the bulk modulus B, and the Debye temperature Θ_D, with structural energy differences, elastic constants, and phonons poorly described in general. In particular, the

TABLE II. Calculated physical properties of bulk bcc Mo, as obtained via the model GPT: (i) in the effective pair-potential approximation defined by Eq. (68) with the coefficients v_a^* and v_b^* treated as free parameters, and (ii) from the multi-ion potentials v_2, v_3, and v_4 with the coefficients v_b and v_d treated as free parameters, but the ratios v_a/v_d, v_c/v_d, and v_e/v_d fixed from Table I. Units: E_{coh} and E_{vac} in Ry, B and elastic constants in Mbar, structural energies in mRy, phonon frequencies in THz, and Θ_D in K. Phonon frequencies are Brillouin-zone-boundary values except as indicated.

	Scheme			
	v_2^{eff}	v_2^{eff}	v_2, v_3, v_4	Experiment
Cohesion				
E_{coh}	−0.643[a]	−0.501[a]	−0.643[a]	−0.501[d]
B	2.64[a]	2.64[a]	2.64[a]	2.64[e]
Vacancy formation				
E_{vac}	0.27	0.35	0.21	0.23[f]
Structural phase stability				
bcc-fcc	−4.3	−5.2	−15.4	−17.5[g]
hcp-fcc	0.0	0.0	1.0	1.5
Elastic constants				
C_{11}	2.62	2.80	3.91	4.66[e]
C_{44}	2.53	1.82	0.80	1.10
C_{12}	2.65	2.57	2.01	1.63
C'	−0.04	0.23	0.95	1.52
Phonons				
L[ζ00][b]	8.05	7.49	7.38	7.61[h]
L[100]	9.80	8.47	6.40	5.52
L[110]	10.20	9.51	5.97	8.14
T_1[110]	c	1.51	4.80	5.73
T_2[110]	7.12	6.03	2.95	4.56
Θ_D	c	372	305	367

[a]Fixed or fitted quantity; $E_{coh} = -0.643$ is the cohesive energy obtained in first-principles GPT calculations using Eqs. (36)–(38) but neglecting *sp-d* hybridization.
[b]In L[ζ00], $\zeta = \frac{3}{5}$.
[c]Imaginary phonon frequencies.
[d]Reference 20.
[e]Room-temperature data of Ref. 21.
[f]Average value from the data of Refs. 22–24.
[g]Estimates of Ref. 25 from thermophysical alloy data.
[h]Room-temperature data of Ref. 26.

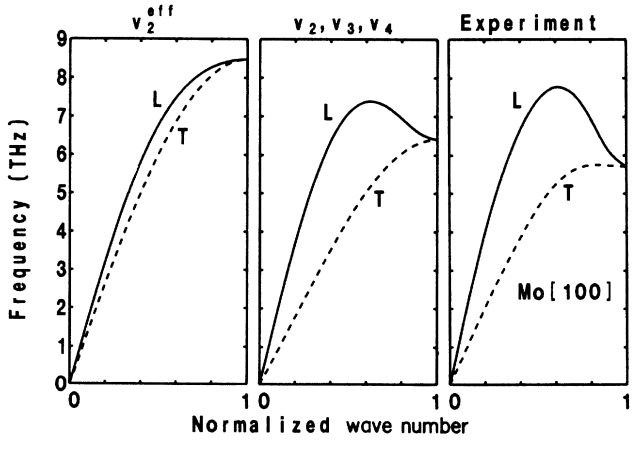

FIG. 10. Longitudinal- (L) and transverse- (T) phonon branches for bcc Mo in the [100] direction, as calculated from the model GPT using the same potential parameters as in Table II. Left, center, and right panels correspond to the second, third, and fourth columns of that table. Experimental curves are from Ref. 26.

multi-ion potentials are necessary to obtain such important group-VI*B* transition-metal properties as (i) the large bcc-fcc energy difference; (ii) the large C' shear elastic constant,

$$C' = \tfrac{1}{2}(C_{11} - C_{12}) > C_{44} \ , \tag{69}$$

and the corresponding stiffening of the transverse T_1-phonon branch above the T_2 branch in the [110] direction (also see Fig. 4 of Ref. 11); and (iii) the large separation between the longitudinal L-phonon branch and the transverse T branch in the [100] direction (corresponding to $C_{11} \gg C_{44}$) and the peaking of the L branch towards the center of the Brillouin zone. The latter is illustrated more clearly for Mo in Fig. 10, where the importance of v_3 and v_4 in obtaining the correct shape of the [100] L and T branches is explicitly demonstrated. More generally, see Ref. 11 and Fig. 21 of Ref. 10.

In applying the interatomic potentials of the model GPT to the calculation of physical properties, it is convenient and appropriate to include a smooth Gaussian cutoff of the functions $f(r)$ and $v_2^{sp}(r)$ at large r. We

have found that one may do this for $f(r)$ quite generally by replacing Eq. (44) with

$$f(r)=\begin{cases}(r_0/r)^p, & r<R_0\\ (r_0/r)^p\exp[-\alpha(r/R_0-1)^2], & r>R_0\end{cases}, \tag{70}$$

terminated past the second-nearest-neighbor distance in the bcc structure. We also assume that v_2 is damped at long range in the same manner as v_2^d, so that, for $r>R_0$, $v_2(r)$ is replaced by $v_2(r)\exp[-2\alpha(r/R_0-1)^2]$. The latter replacement has negligible effect on $v_2^{\rm hc}$, but has the physically correct effect of suppressing the weak Friedel oscillations contained in v_2^{sp}. This cutoff scheme for $f(r)$ and $v_2(r)$ has been used here in the results presented in Table II and in all of the model-GPT results to be discussed in Sec. IV. Additional information on the calculation of physical properties from the multi-ion potentials is also given in Sec. IV.

IV. FULL APPLICATION TO MOLYBDENUM

We now consider the detailed application of the model GPT to the calculation of accurate physical properties in the central transition metals. We continue to confine our attention to the representative case of Mo, where a great deal of complementary first-principles calculational data exists that is useful in seeking optimum values for the potential coefficients v_a, v_b, v_c, v_d, and v_e. In addition to first-principles GPT results, we have available a parallel set of self-consistent local-density-approximation (LDA) total-energy calculations on fcc and bcc Mo (Refs. 10 and 27–29) obtained using the linear muffin-tin orbital (LMTO) band-structure method.[13,15] These calculations have been done over a wide volume range ($0.30\le\Omega/\Omega_0\le 1.15$, where $\Omega_0=105.1$ a.u. is the observed equilibrium atomic volume for bcc Mo), and provide accurate LDA data on both cohesive properties (cohesive energy $E_{\rm coh}$, pressure P, and bulk modulus B) and bcc-fcc and hcp-fcc structural energy differences. The LMTO results are also in excellent agreement with experiment with regard to the predicted zero-pressure volume and bulk modulus plus the equation of state $P(\Omega)$ below 2 Mbar. Independently, other workers have calculated high-symmetry phonons for bcc Mo at normal density ($\Omega=\Omega_0$) within the LDA using *ab initio* pseudopotentials and a frozen-phonon total-energy technique.[30,31]

Our basic strategy in determining the d-state-potential coefficients is as follows. From the analysis of Sec. III, we fix the decay-law power in the radial function $f(r)$ at $p=4$ and the ratio of v_c to v_d at $v_c/v_d=-0.1937$ (Table I). This ensures that the *shapes* of v_3 and v_4 are maintained exactly as in Figs. 5 and 8 and hence are always good approximations to the first-principles GPT potentials regardless of the choice of the other parameters. Moreover, as a practical matter there is not much leverage to be gained in varying either p or v_c/v_d, as can be inferred from Table I and the fact that v_c in Mo is inherently small. Next, we fit the four remaining coefficients v_a, v_b, v_d, and v_e to four calculated or experimental physical properties at normal density, at least one of which is always the LMTO bulk modulus $B=2.64$ Mbar. The fitting procedure is extended to higher and lower volumes by imposing the theoretical constraints that v_a/v_d and v_e/v_d are independent of volume, as in Eqs. (65) and (66), and then determining v_b and v_d from the LMTO values of $E_{\rm coh}(\Omega)-E_{\rm coh}(\Omega_0)$ and $B(\Omega)$ such that the compressibility sum rule

$$B\equiv\Omega\frac{\partial^2 E_{\rm coh}}{\partial\Omega^2}=(C_{11}+2C_{12})/3 \tag{71}$$

is exactly satisfied at each volume. The second equality in Eq. (71) is achieved by calculating B in the model GPT from the elastic constants C_{11} and C_{12} obtained via radial and angular derivatives of the interatomic potentials v_2, v_3, and v_4 at constant volume. To fit $E_{\rm coh}(\Omega)-E_{\rm coh}(\Omega_0)$, which ensures that the first equality in Eq. (71) is satisfied, we require the volume term $E_{\rm vol}(\Omega)$ in Eq. (30) to calculate $E_{\rm coh}(\Omega)$ within the model GPT. In the present work, we utilize the $E_{\rm vol}(\Omega)$ we have calculated from the first-principles GPT in the limit of no *sp-d* hybridization (beyond that implicit in $E_{\rm vol}^d$). This is consistent with the approximations made in the model-GPT formalism of Sec. III, although the optimum choice of volume term is still a matter for further investigation. In any case, $E_{\rm vol}(\Omega)$ controls only the volume dependence of v_b and v_d directly and *not* the values of the potential coefficients at Ω_0. Thus the only normal-density physical properties affected by this function are $E_{\rm coh}(\Omega_0)$ and volume or pressure derivatives.

Our general fitting procedure ensures that, apart from the additive constant in $E_{\rm coh}(\Omega_0)$, the accurate cohesive properties of the LMTO calculations are automatically built into the model-GPT results. At the same time, we still maintain the flexibility of choosing three remaining free parameters. We have considered a number of different schemes to determine these remaining parameters and all give very similar results. Here we will discuss the results obtained from five specific schemes which give a fairly representative sample of what is possible within this framework. Calculated physical properties from these five schemes and the particular properties fitted are summarized in Table III. In addition to cohesive properties, we include results on the vacancy-formation energy and volume, bcc-fcc and hcp-fcc energy differences plus the predicted transition pressure for the recently discovered bcc→hcp phase transition,[27] elastic constants and their pressure derivatives, and phonon frequencies and their averages. We now proceed to discuss these results in turn.

For simplicity, we have treated vacancy formation in the unrelaxed bcc lattice at constant volume, since relaxation effects and other corrections are estimated to be quite small for Mo. The unrelaxed vacancy-formation energy at constant volume, $E_{\rm vac}$, may be thought of as arising from a two-step process: (i) a bulk atom is removed from the interior of the metal and placed on the surface, and (ii) the metal is then uniformly compressed to maintain constant volume. This gives rise to both

TABLE III. Calculated physical properties of bulk bcc Mo, as obtained from the model GPT in five schemes with the multi-ion-potential coefficients v_a, v_b, v_d, and v_e treated as free parameters. Units: E_{coh} and E_{vac} in Ry, B, $P_{bcc\to hcp}$, and elastic constants in Mbar, structural energies in mRy, phonon frequencies in THz, and Θ_D in K. Phonon frequencies are Brillouin-zone-boundary values except as indicated.

	Scheme						
	1	2	3	4	5	Experiment	Band theory
Cohesion							
E_{coh}	−0.664	−0.700	−0.643[a]	−0.499	−0.649	−0.501[c]	−0.455[d]
B	2.64[a]	2.64[a]	2.64[a]	2.64[a]	2.64[a]	2.64[e]	2.64
Vacancy formation							
E_{vac}	0.23[a]	0.20	0.24	0.35	0.23[a]	0.23[f]	
Ω_{vac}/Ω_0	0.79	0.79	0.79	0.75	0.79		
Structural phase stability							
bcc-fcc	−19.8	−20.2	−18.0	−14.7	−16.1	−17.5[g]	−30.0[d]
hcp-fcc	2.0	2.0	1.7	1.3	1.3	1.5	2.0
$P_{bcc\to hcp}$	3.5	3.7	3.4	2.1	3.3	>2.7[h]	3.2
Elastic constants							
C_{11}	4.66[a]	4.66[a]	4.44	4.11	4.10	4.66[e]	
C_{44}	1.10[a]	1.10[a]	1.18	1.04	1.15	1.10	
C_{12}	1.63	1.63	1.74	1.91	1.91	1.63	
C'	1.51	1.51	1.35	1.10	1.09	1.52	
Pressure derivatives							
$\partial B/\partial P$	4.42	4.42	4.42	4.42	4.42	4.44[i]	4.42[d]
$\partial C_{11}/\partial P$	5.30	5.30	5.21	5.02	5.10	6.41	
$\partial C_{44}/\partial P$	1.38	1.38	1.41	1.39	1.40	1.40	
$\partial C_{12}/\partial P$	3.99	3.98	4.03	4.12	4.09	3.45	
$\partial C'/\partial P$	0.65	0.66	0.59	0.45	0.50	1.48	
Phonon frequencies							
L[ζ00][b]	9.02	8.95	8.84	8.43	8.26	7.61[j]	
L[100]	8.42	8.33	8.40	7.96	7.84	5.52	5.0[k]
L[110]	7.26	6.95	7.55	8.12	7.22	8.14	
T_1[110]	6.16	6.16	5.80[a]	5.20[a]	5.20[a]	5.73	5.8[l]
T_2[110]	3.67	3.59	4.00[a]	4.00[a]	4.00[a]	4.56	4.0[l]
L[$\xi\xi\xi$][b]	6.25	6.24	6.04	5.53	5.56	6.16	6.1[k]
Phonon averages							
Θ_D	373	367[a]	375	367[a]	356	367[j]	
γ_G	1.53	1.58	1.46	1.46	1.55	1.55[i]	

[a]Fixed or fitted quantity.
[b]In L[ζ00], $\zeta=\frac{3}{5}$; in L[$\xi\xi\xi$], $\xi=\frac{2}{3}$.
[c]Reference 20.
[d]Parallel LMTO results: Refs. 10, 27–29.
[e]Room-temperature data of Ref. 21.
[f]Average value from the data of Refs. 22–24.
[g]Estimates of Ref. 25 from thermophysical alloy data.
[h]Room-temperature data of Ref. 36.
[i]Room-temperature data of Ref. 37.
[j]Room-temperature data of Ref. 26.
[k]Reference 30.
[l]Reference 31.

cohesive-energy and virial-pressure contributions to E_{vac}, so that in the present context one may write

$$E_{vac}=E_{vac}^{(2)}+E_{vac}^{(3)}+E_{vac}^{(4)}\ , \tag{72}$$

where

$$E_{vac}^{(n)}=-(n-1)E_{coh}^{(n)}+\Omega P_{vir}^{(n)}\ , \tag{73}$$

with

$$E_{coh}^{(n)}\equiv\frac{1}{N\,n!}\sum_{i,j,\ldots}{}'\ v_n(i,j,\ldots) \tag{74}$$

and

$$P_{vir}^{(n)}\equiv-\frac{1}{6N\Omega\,(n-2)!}\sum_{i,j,\ldots}{}'\ R_{ij}\frac{\partial}{\partial R_{ij}}[v_n(i,j,\ldots)]\ . \tag{75}$$

Table IV lists calculated components of the cohesive and vacancy-formation energies of Mo so obtained from the model GPT within our five schemes. Except in the atypical case of scheme 4, there are very small net contributions to E_{vac} from the two- and four-ion potentials, and the result is dominated by three-ion-potential contributions, and, as shown in Table III, good overall agreement with experiment is obtained, *except* in scheme 4. Although the cohesive energy is dominated by E_{vol} and v_2 as opposed to v_3, it is interesting to note that there is a

TABLE IV. Cohesive and vacancy-formation energies and their components for Mo at normal density ($\Omega=\Omega_0$), as calculated via the model GPT for the five schemes of Table III. Energies in Ry.

	E_{vol}	v_2	v_3	v_4	Total
Scheme 1					
E_{coh}	−0.42	−0.31	0.08	−0.01	−0.66
E_{vac}		−0.01	0.26	−0.03	0.23
Scheme 2					
E_{coh}	−0.42	−0.36	0.09	−0.01	−0.70
E_{vac}		−0.06	0.29	−0.03	0.20
Scheme 3					
E_{coh}	−0.42	−0.28	0.07	−0.01	−0.64
E_{vac}		0.03	0.23	−0.02	0.24
Scheme 4					
E_{coh}	−0.42	−0.11	0.04	−0.01	−0.50
E_{vac}		0.23	0.14	−0.02	0.35
Scheme 5					
E_{coh}	−0.42	−0.29	0.07	−0.01	−0.65
E_{vac}		0.01	0.24	−0.02	0.23

strong inverse relationship between the magnitudes of E_{coh} and E_{vac}. When the magnitude of E_{coh} is calculated to be in the vicinity of its first-principles GPT value ($E_{coh}=-0.643$ Ry), then E_{vac} is maintained close to the average experimental value of 0.23 Ry, as in schemes 1–3 and 5. If, on the other hand, the calculated magnitude of E_{coh} is significantly less, as in scheme 4, then E_{vac} is increased accordingly.

The corresponding vacancy-formation volume Ω_{vac} may be calculated from the bulk modulus and the first volume derivative of E_{vac} according to

$$\Omega_{vac}/\Omega_0=-B^{-1}\frac{\partial E_{vac}}{\partial\Omega}\ . \tag{76}$$

Not unexpectedly, we always obtain $\Omega_{vac}/\Omega_0<1$, and as seen in Table III the calculated value of Ω_{vac} is quite insensitive to the details of any particular scheme. Instead, the variable factor most influencing the magnitude of this quantity is the volume dependence of the volume term $E_{vol}(\Omega)$. The general qualitative relationship we find is that a decrease in the value of $\partial E_{vol}/\partial\Omega$ at Ω_0 will also decrease Ω_{vac}/Ω_0.

Structural energy differences among the fcc, bcc, and hcp structures are conveniently calculated at constant volume so that only v_2, v_3, and v_4 contribute to the results. The extreme stability of the bcc structure at normal density in the central transition metals is maintained by both v_2 and v_4. As shown in Table V, the total bcc-fcc energy difference contains large and approximately equal contributions from the two- and four-ion potentials for Mo in all five of our schemes. The range of values obtained for the bcc-fcc energy difference (−14.7 mRy in scheme 4 to −20.2 mRy in scheme 2) is in good accord with the empirical estimate of −17.5 mRy by Miedema

TABLE V. bcc-fcc and hcp-fcc structural-energy differences and their components for Mo at normal density ($\Omega=\Omega_0$), as calculated via the model GPT for the five schemes of Table III. Energies in mRy.

	v_2	v_3	v_4	Total
Scheme 1				
bcc-fcc	−11.0	3.9	−12.8	−19.8
hcp-fcc	0.0	−0.3	2.2	2.0
Scheme 2				
bcc-fcc	−11.7	4.4	−12.9	−20.2
hcp-fcc	0.0	−0.3	2.3	2.0
Scheme 3				
bcc-fcc	−10.3	3.5	−11.2	−18.0
hcp-fcc	0.0	−0.2	2.0	1.7
Scheme 4				
bcc-fcc	−8.4	2.0	−8.4	−14.7
hcp-fcc	0.0	−0.1	1.5	1.3
Scheme 5				
bcc-fcc	−10.8	3.5	−8.8	−16.1
hcp-fcc	0.0	−0.2	1.6	1.3

and Niessen[25] obtained on the basis of extrapolating thermophysical alloy data, but somewhat less (in magnitude) than the value of -30.0 mRy we have obtained from our LMTO calculations.[10,27–29] A more recent attempt to refine the empirical extrapolation[32] lessens the latter discrepancy only slightly, giving a value of -21.3 mRy, while other LDA band-structure calculations of the bcc-fcc energy difference[33–35] are in good accord with our LMTO result. The much smaller hcp-fcc energy difference, on the other hand, is dominated almost entirely by v_4 in the model GPT and, for all five of our schemes, is in good accord, both in sign and magnitude, with that of Miedema and Niessen as well as the LMTO calculations.

All five of our model-GPT schemes also correctly display the observed destabilization of the bcc structure at high pressure, an effective driven by $s \rightarrow d$ electron transfer[27,28] and manifest here through the volume dependence of the d-state-potential coefficients. Our parallel LMTO calculations predict a bcc→hcp transition at about 3.2 Mbar and zero temperature, while shock measurements reveal that the bcc structure destabilizes at 2.1 Mbar and very high temperature (approximately 4100 K).[27] A more recent static experimental study at room temperature,[36] however, shows that the bcc structure is still stable at 2.7 Mbar, so that the low-temperature bcc→hcp transition is presumably above this pressure. As shown in Table III, our model-GPT calculations give transition pressures of 2.1 Mbar for scheme 4 and in the narrow range of 3.3–3.7 Mbar for the other four schemes. Relative to the LMTO result, the latter values represent a significant improvement over our initial model-GPT estimate of 2.2 Mbar reported in Ref. 11 and obtained with a preliminary version of scheme 5, but a less accurate form of the volume term $E_{\rm vol}$, which influences the quantitative result substantially. Actually, the model GPT will predict either a bcc→hcp or a bcc→fcc transition, depending on the details of the calculation. However, the hcp-fcc energy difference is always so small at the point of the transition that we do not regard this as especially significant and we have ignored this difference in Table III. In Ref. 11 and the present scheme 4, the predicted transition is bcc→hcp, while in the present schemes 1–3 and 5 the transition is bcc→fcc.

The calculation of elastic constants and phonons at constant volume requires first and second derivatives of the potentials v_2, v_3, and v_4. The usual force constants of harmonic lattice dynamics may be expressed, through chain-rule differentiation, in terms of generalized radial and tangential force-constant functions defined by the expressions

$$K_t^{(n)}(\alpha,\beta) \equiv (R_{\alpha\beta})^{-1} \frac{\partial v_n(i,j,\ldots)}{\partial R_{\alpha\beta}} \tag{77}$$

and

$$K_r^{(n)}(\alpha,\beta,\gamma,\delta) \equiv \frac{\partial^2 v_n(i,j,\ldots)}{\partial R_{\alpha\beta}\partial R_{\gamma\delta}} , \tag{78}$$

respectively, for the potential v_n. In principle, such derivatives of the multi-ion potentials v_3 and v_4 may always be calculated analytically within the model GPT. In practice, we have succeeded in doing this for v_3 but not yet for v_4, where the result becomes algebraically complicated, especially for the second derivatives. An attractive and useful alternative, however, is to calculate the derivatives numerically, exploiting the fact that the potentials themselves are analytic by using arbitrarily small displacements of the ion positions to obtain high accuracy. As a practical matter, all numerical derivatives may be so calculated with great computational speed and no significant error.

The model GPT yields good values of the elastic constants for group-VIB metals so long as a good value for the bulk modulus B is maintained. Thus in the present work our five schemes generally give proper magnitudes as well as interrelationships among the elastic constants [e.g., $C_{11} \gg C_{44}$ and $C' > C_{44}$ (except scheme 5)], even though this is only guaranteed in schemes 1 and 2. This good agreement with experiment is also extended to the pressure derivatives of B and the elastic constants,[37] as demonstrated in Table III. The pressure derivatives of the elastic constants are influenced to a moderate extent by the volume term $E_{\rm vol}$. The remaining quantitative differences for $\partial C_{11}/\partial P$, $\partial C_{12}/\partial P$, and $\partial C'/\partial P$ can be lessened or possibly removed entirely with a decrease in the value of $\partial E_{\rm vol}/\partial\Omega$ at Ω_0.

The model GPT generally produces a qualitatively correct phonon spectrum in our five schemes, with the major quantitative discrepancy again being the underestimate of the softening of the [100] zone-boundary phonons. In fact, agreement with experiment for the L[100] phonon is worsened somewhat in all five schemes over the results given in Table II and Fig. 10. Otherwise, however, good quantitative agreement with both experiment[26] and with the frozen-phonon LDA calculations[30,31] is maintained. Each of our model-GPT schemes also gives good phonon averages, as measured by the Debye temperature Θ_D and the Grüneisen parameter γ_G. We define the former in terms of the calculated zero-point vibrational energy

$$E_{\rm ph}^0 = \frac{1}{2N} \sum_{\mathbf{q},\lambda} h\nu_\lambda(\mathbf{q}) , \tag{79}$$

according to the Debye formula $E_{\rm ph}^0 \equiv \frac{9}{8} k_B \Theta_D$, while the latter is given by

$$\gamma_G = -\frac{1}{3N} \sum_{\mathbf{q},\lambda} \Omega \frac{\partial \ln[h\nu_\lambda(\mathbf{q})]}{\partial\Omega} . \tag{80}$$

In Eqs. (79) and (80), the summations are over all phonon frequencies $\nu_\lambda(\mathbf{q})$ of wave vector $\mathbf{q}$ and branch λ in the Brillouin zone.

Finally, it is of interest to mention briefly the behavior of our fitted d-state potential coefficients in our five model-GPT schemes. These results are summarized in Table VI in the form of the ratios v_a/v_d, v_b/v_d, v_c/v_d, and v_e/v_d, and should be compared with the corresponding values in Table I. The ratios for schemes 1–3 and 5 are seen to be remarkably similar, while those for scheme 4 display a much smaller value of v_a/v_d and a larger value of v_e/v_d. Relative to the coefficients for the fitted first-principles GPT potentials in Table I, v_a/v_d, v_b/v_d,

TABLE VI. Ratios of d-state-potential coefficients obtained from the five model-GPT schemes of Table III.

	Scheme				
	1	2	3	4	5
v_a/v_d	2.660	2.797	2.894	0.5780	2.673
v_b/v_d	31.37	31.52	33.26	29.90	33.35
v_c/v_d	−0.1937	−0.1937	−0.1937	−0.1937	−0.1937
v_e/v_d	4.690	4.282	4.681	5.945	3.628

and v_e/v_d for the former schemes have been increased by roughly a factor of 2 in each case. This means that, except in scheme 4, v_a/v_b and hence the *shape* of v_2^d are essentially the same as that of the corresponding first-principles GPT potential (Fig. 2). This leads to the interesting and very satisfying conclusion that so long as one approximately preserves the *magnitude* of the first-principles GPT cohesive energy (as is done in schemes 1–3 and 5), then our general fitting procedure also preserves the *shapes* of the first-principles d-state potentials v_2^d, v_3^d, and v_4^d.

V. CONCLUSIONS

Many additional applications of the model-GPT formalism developed in Sec. III should be possible for the central transition metals. In particular, the analytic nature of the multi-ion potentials in the model GPT make this approach compatible with molecular-dynamics and Monte Carlo computer-simulation methods, so that more general materials properties can be studied. Prime examples of problems which could be so addressed with the present potentials include the energetics of point and line defects, the atomic structure of grain boundaries, melting and liquid-metal properties, and pressure-temperature phase diagrams. In this regard, a useful package of data and computer subroutines which can assist the interested reader in implementing the model GPT is available from the author upon request. The general type of fitting procedure we have developed for determining the d-state potential coefficients in the case of Mo can readily be applied to other central transition metals. We have made preliminary attempts to do this in the metals Cr, V, and Nb at normal density with comparable success.

One possible refinement in the model GPT for the future, which could increase the flexibility of the approach without compromising its analytic nature, is to remove the assumption of pure canonical d bands in defining the three- and four-ion angular functions L, P, and M. The ideal ratios of $6{:}(-4){:}1$ for canonical d bands can be replaced by arbitrary constant ratios of $S{:}P{:}D$ and corresponding angular functions defined. This effectively allows two additional material-dependent parameters (S/P and S/D) at no significant cost in the complexity of the theory. To date we have so obtained generalized three-ion functions L and P in analytic form, but not a generalized form of the four-ion function M.

We are also currently attempting to expand the capabilities of the GPT beyond bulk elemental metals. Very recently, we have succeeded in extending the transition-metal GPT to surfaces[38] by making an internal transformation of the cohesive-energy functional to an embedded-atom-like[39] or effective-medium-like[40] representation, in which the embedding function is identified as the bulk volume term $E_{\rm vol}$, and the atomic volume Ω is replaced by an environmentally averaged electron density. The bulk interatomic potentials are otherwise transferable to the surface, so that all of the desirable features of the model GPT developed here can be used for surface calculations as well. Beyond elemental metals, it should be further possible to extend both the first-principles and model GPT to compounds and alloys, as has been done successfully by Hafner[5] for nontransition metals within the framework of simple-metal pseudopotential theory.

ACKNOWLEDGMENTS

This work was performed, under the auspices of the U.S. Department of Energy, by Lawrence Livermore National Laboratory under Contract No. W-7405-Eng-48.

APPENDIX A

In this Appendix we elaborate a few selected technical details of the first-principles GPT formalism which are relevant to the discussion in Sec. II and also to the applications of the model GPT to Mo in Secs. III and IV. Following Ref. 10, one may include in the definition of the self-consistent electron potential V an arbitrary constant $-V_0$ which determines the zero of energy. One must then add an explicit term ZV_0 to the valence-binding energy (26) to ensure that V_0 cancels out in this quantity. The constant V_0 does affect, however, the definition of the zeroth-order pseudoatom through Eqs. (7), (17), and (18). The atomic reference potential entering Eq. (7) has the form

$$v_{\rm at}(r)=v_{\rm pa}(r)+v_{\rm loc}(r)-V_0' \tag{A1}$$

where V_0' is the constant

$$V_0'\equiv V_0-\mu_{\rm xc}(n_{\rm unif})\ , \tag{A2}$$

with $n_{\rm unif}\equiv Z/\Omega$. Here, $v_{\rm pa}$ and $v_{\rm loc}$ are, respectively, the self-consistent pseudoatom potential and a fixed repulsive barrier potential which shapes the tails of the localized d states $|\phi_d\rangle$, as discussed in Refs. 7 and 10. The d-state energy $E_d^{\rm vol}$ entering the phase shift (17) then has the form

$$E_d^{\rm vol}=E_d^{\rm pa}-\langle\phi_d|\delta V_{\rm unif}|\phi_d\rangle-V_0'\ , \tag{A3}$$

where $E_d^{\rm pa} \equiv \langle \phi_d | (T + v_{\rm pa} + v_{\rm loc}) | \phi_d \rangle$ and $-\delta V_{\rm unif}$ is the additional Coulomb potential arising from the uniform electron density outside the atomic sphere of the pseudoatom, as also discussed in Refs. 7 and 10. The effective strength of $v_{\rm loc}$ is specified through the logarithmic derivative

$$D_2^* \equiv R_{\rm WS} \frac{\partial}{\partial r} [\ln \mathcal{R}_2(R_{\rm WS}, E_d^{\rm vol})] , \tag{A4}$$

where $\mathcal{R}_2(r,E)$ is the solution to the radial Schrödinger equation associated with Eq. (7) for $r < R_{\rm WS}$.

The constant V_0' similarly appears in the nearly-free-electron valence-energy levels through the diagonal pseudopotential matrix element

$$\langle \mathbf{k} | w_{\rm pa} | \mathbf{k} \rangle = \langle \mathbf{k} | v_{\rm pa} | \mathbf{k} \rangle - V_0' + \sum_c (\varepsilon_{\mathbf{k}} - E_c^{\rm vol}) \langle \mathbf{k} | \phi_c \rangle \langle \phi_c | \mathbf{k} \rangle , \tag{A5}$$

where $E_c^{\rm vol}$ are inner-core-state energies analogous to Eq. (A3) for $E_d^{\rm vol}$:

$$E_c^{\rm vol} = E_c^{\rm pa} - \langle \phi_c | \delta V_{\rm unif} | \phi_c \rangle - V_0' . \tag{A6}$$

The value of

$$w_0 \equiv \langle 0 | w_{\rm pa} | 0 \rangle \tag{A7}$$

establishes the location of the bottom of the valence-energy bands relative to the zero of energy. Combining Eqs. (A5)–(A7) gives the constant V_0' in terms of w_0:

$$V_0' = \frac{\langle 0 | v_{\rm pa} | 0 \rangle - w_0 - \sum_c (E_c^{\rm pa} - \langle \phi_c | \delta V_{\rm unif} | \phi_c \rangle) \langle 0 | \phi_c \rangle \langle \phi_c | 0 \rangle}{1 - \langle 0 | p_c | 0 \rangle} , \tag{A8}$$

where p_c is the usual inner-core-state projection operator $\sum_c |\phi_c\rangle\langle\phi_c|$. The pseudopotential $w_{\rm pa}'$ entering the zeroth-order pseudoatom cohesive energy (34) is just

$$w_{\rm pa}' \equiv w_{\rm pa} + V_0' , \tag{A9}$$

for which V_0 cancels out, as it must.

The effective variable parameters of the zeroth-order pseudoatom are D_2^* and w_0 (or V_0'). The nominal default values for these quantities are $D_2^* = -3$, the canonical d-band condition fixing $E_d^{\rm vol}$ at the center of the d bands, and $w_0 = 0$, the condition placing the zero of energy at the bottom of the valence-energy bands. In Ref. 10 both of these conditions were normally maintained, except that we noted that values of D_2^* closer to -2 were more nearly optimum for the central transition metals. In practice, D_2^* and V_0' are fine-tuning "knobs" which can be used to advantage, if desired. In the present applications to Mo, we use this flexibility to make our zeroth-order pseudoatom completely consistent with the parallel LMTO band-structure data[10,27–29] we use in connection with establishing the d-state potential coefficients in the model GPT. Specifically, we have chosen D_2^* and V_0' such that the zeroth-order pseudoatom reproduces the calculated LMTO values of Z_d and W_d. In this regard, we have found that to a good approximation the single value $D_2^* = -2.15$ gives the LMTO d-band width W_d at all volumes Ω when V_0' is adjusted at each volume to yield the desired LMTO value of Z_d. At normal density ($\Omega = \Omega_0$), we so obtain $Z = 1.402$ and $Z_d = 4.598$; these values are maintained throughout Secs. III and IV.

APPENDIX B

To obtain analytic expressions for the multi-ion angular functions L, P, and M, one begins by defining these functions in terms of the familiar 5×5 Slater-Koster tight-binding matrix for d states coupling two sites.[41,42] Let $H(i,j)$ be such a Slater-Koster matrix coupling sites i and j with the parameters $S \equiv dd\sigma = 6$, $P \equiv dd\pi = -4$, and $D \equiv ddd = 1$. Then,

$$L(x_1,x_2,x_3) \equiv \tfrac{1}{90} {\rm Tr}[H(1,2)H(2,3)H(3,1)] , \tag{B1}$$

where $90 = S^3 + 2P^3 + 2D^3$,

$$P(x_3) \equiv \tfrac{1}{1810} {\rm Tr}[H(1,2)H(2,1)H(2,3)H(3,2)] , \tag{B2}$$

and, for configuration (a) of Fig. 6,

$$M(x_1,x_2,x_3,x_4,x_5,x_6) \equiv \tfrac{1}{1810} {\rm Tr}[H(1,2)H(2,3)H(3,4)H(4,1)] , \tag{B3}$$

where $1810 = S^4 + 2P^4 + 2D^4$. Straightforward evaluation of Eqs. (B1) and (B2) yields Eqs. (50) and (51) for L and P, respectively, noting $144 = \frac{8}{5}(90)$ and $1448 = \frac{4}{5}(1810)$. The four-ion angular function M can be developed in the form

$$M(x_1,x_2,x_3,x_4,x_5,x_6) = \tfrac{1}{5792}[T_1 + 5x_2^2(T_2 + x_2^2 T_3) + 10 s_2 x_2 (T_4 + x_2^2 T_5)] , \tag{B4}$$

where $5792 = \frac{16}{5}(1810)$,

$$s_n \equiv (1 - x_n^2)^{1/2} , \tag{B5}$$

and the T_n are functions of the x_n and s_n. The angles θ_n in Fig. 6 are defined to lie in the range of $0 \le \theta_n \le \pi$, in which case $s_n = \sin(\theta_n) \ge 0$. It is convenient to express the T_n as terms of the direction cosines l_i, m_i, and n_i defining the four vectors $\mathbf{R}_{ij}$ such that $\mathbf{R}_{12} = (l_1 \hat{\mathbf{x}} + m_1 \hat{\mathbf{y}} + n_1 \hat{\mathbf{z}}) r_1$, etc.[43] If one chooses $l_1 = m_1 = 0$ and $n_1 = 1$, and $l_2 = s_2$, $m_2 = 0$, and $n_2 = -x_2$, then it readily follows that

$$l_3=-(x_2x_6+x_1x_5)/(x_2s_5+x_5s_2)\ , \tag{B6}$$

$$n_3=(x_1s_5-x_6s_2)/(x_2s_5+x_5s_2)\ , \tag{B7}$$

$$l_4=(x_3x_5+x_4x_6-s_4s_6)/s_5\ , \tag{B8}$$

$$n_4=-x_3\ , \tag{B9}$$

and $m_3=-m_4=(1-l_3^2-n_3^2)^{1/2}$. In the limiting case $s_2=0$, then $l_3=s_1$, $n_3=x_1/x_2$, and $l_4=-s_3$. In terms of l_3, n_3, l_4, n_4, and x_4, the T_n in Eq. (B4) are found to be

$$\begin{aligned}T_1\equiv&-258+2415(l_3^2+n_4^2)+165(l_4^2+n_3^2)-945(l_3^2l_4^2+n_3^2n_4^2)-2415(l_3^4+n_4^4)+210(l_4^4+n_3^4)-2415(l_3^2n_3^2+l_4^2n_4^2)\\&-21\,795l_3^2n_4^2+705l_4^2n_3^2-1470(l_3^2l_4^4+l_3^4l_4^2+n_3^2n_4^4+n_3^4n_4^2)+20\,790(l_3^4n_4^2+l_3^2n_4^4)-210(l_4^4n_3^2+l_4^2n_3^4)\\&+945(l_3^2l_4^2n_3^2+n_3^2n_4^2l_4^2)+16\,695(l_3^2l_4^2n_4^2+n_3^2n_4^2l_3^2)-47\,775l_3^2l_4^2n_3^2n_4^2-17\,395l_3^4n_4^4+980l_4^4n_3^4\\&+1470(l_3^2l_4^4n_3^2+l_3^4l_4^2n_4^2+l_3^2n_3^2n_4^4+l_4^2n_3^4n_4^2)+l_3l_4n_3n_4[15\,150-22\,470(l_3^2+n_4^2)-17\,220(l_4^2+n_3^2)\\&-2940(l_3^2l_4^2+n_3^2n_4^2)+50\,470l_3^2n_4^2+13\,720l_4^2n_3^2]\\&+x_4l_3l_4(1410-4830l_3^2+420l_4^2+4620n_3^2-11\,130n_4^2-2940l_3^2l_4^2-49\,980n_3^2n_4^2+42\,630l_3^2n_4^2+5880l_4^2n_3^2)\\&+x_4n_3n_4(1410-11\,130l_3^2+4620l_4^2+420n_3^2-4830n_4^2-49\,980l_3^2l_4^2-2940n_3^2n_4^2+42\,630l_3^2n_4^2+5880l_4^2n_3^2)\ ,\end{aligned} \tag{B10}$$

$$\begin{aligned}T_2\equiv&282-3957l_3^2-357l_4^2+1137n_3^2-2463n_4^2+1260l_3^2l_4^2-11\,520n_3^2n_4^2+4158l_3^4-42l_4^4-1785n_3^4+2415n_4^4\\&+2751(l_3^2n_3^2+l_4^2n_4^2)+37\,380l_3^2n_4^2+1380l_4^2n_3^2+2940(l_3^2l_4^4+l_3^4l_4^2)+12\,495(n_3^2n_4^4+n_3^4n_4^2)-37\,380l_3^4n_4^2\\&-36\,855l_3^2n_4^4-3780l_4^4n_3^2-3255l_4^2n_3^4-5040(l_3^2l_4^2n_3^2-n_3^2n_4^2l_4^2)-30\,240l_3^2l_4^2n_4^2-20\,160n_3^2n_4^2l_3^2\\&+126\,420l_3^2l_4^2n_3^2n_4^2+32\,830l_3^4n_4^4+3430l_4^4n_3^4-2940(l_3^2l_4^4n_3^2+l_3^4l_4^2n_4^2)\\&-12\,495(l_3^2n_3^2n_4^4+l_4^2n_3^4n_4^2)+l_3l_4n_3n_4(-41\,730+54\,180l_3^2+45\,780l_4^2+44\,730n_3^2+53\,130n_4^2+5880l_3^2l_4^2\\&+24\,990n_3^2n_4^2-110\,740l_3^2n_4^2-51\,940l_4^2n_3^2)\\&+x_4l_3l_4(-930+7140l_3^2-1260l_4^2-14\,910n_3^2+10\,290n_4^2+5880l_3^2l_4^2+130\,830n_3^2n_4^2-67\,620l_3^2n_4^2-8820l_4^2n_3^2)\\&+x_4n_3n_4(1230+17\,220l_3^2-7980l_4^2-8610n_3^2-210n_4^2+99\,960l_3^2l_4^2+24\,990n_3^2n_4^2-73\,500l_3^2n_4^2-14\,700l_4^2n_3^2)\ ,\end{aligned} \tag{B11}$$

$$\begin{aligned}T_3\equiv&196+2800l_3^2-350l_4^2-4760n_3^2-1610n_4^2+105l_3^2l_4^2+35\,805n_3^2n_4^2-3479l_3^4\\&+196l_4^4+5341n_3^4+1666n_4^4+1274(l_3^2n_3^2+l_4^2n_4^2)-28\,805l_3^2n_4^2+2695l_4^2n_3^2\\&-3430(l_3^2l_4^4+l_3^4l_4^2)-29\,155(n_3^2n_4^4+n_3^4n_4^2)+32\,830l_3^4n_4^2+29\,155l_3^2n_4^4\\&+3430l_4^4n_3^2-245l_4^2n_3^4+3675(l_3^2l_4^2n_3^2-n_3^2n_4^2l_3^2)+25\,725(l_3^2l_4^2n_4^2-n_3^2n_4^2l_4^2)-142\,345l_3^2l_4^2n_3^2n_4^2\\&-29\,155l_3^4n_4^4-3430l_4^4n_3^4+3430(l_3^2l_4^4n_3^2+l_3^4l_4^2n_4^2)+29\,155(l_3^2n_3^2n_4^4+l_4^2n_3^4n_4^2)\\&+l_3l_4n_3n_4[50\,680-62\,230l_3^2-47\,530n_3^2-54\,880(l_4^2+n_4^2)-6860l_3^2l_4^2-58\,310n_3^2n_4^2+113\,190l_3^2n_4^2+61\,740l_4^2n_3^2]\\&+x_4l_3l_4[-700-5390l_3^2+1960l_4^2+21\,070n_3^2-980n_4^2-6860l_4^2(l_3^2-n_3^2)-168\,070n_3^2n_4^2+58\,310l_3^2n_4^2]\\&+x_4n_3n_4[-9100-8330l_3^2+13\,720l_4^2+24\,010n_3^2+16\,660n_4^2-116\,620l_3^2l_4^2+58\,310n_4^2(l_3^2-n_3^2)+6860l_4^2n_3^2]\ ,\end{aligned} \tag{B12}$$

$$\begin{aligned}T_4\equiv&l_3n_3[-972+1113l_3^2+1155n_3^2+105l_4^2+8535n_4^2+1470l_4^2(l_3^2+l_4^2)\\&-6615l_4^2n_4^2-8085n_4^2(n_3^2+n_4^2)+945l_4^2n_3^2-8610l_3^2n_4^2-1470l_4^4n_3^2+8085l_3^2n_4^4-13\,230l_3^2l_4^2n_4^2+13\,965n_3^2n_4^2l_4^2]\\&+l_4n_4[-522+5880l_3^2-1740n_3^2+588l_4^2+630n_4^2-5880l_3^2(l_3^2+l_4^2+n_4^2)+2940n_3^2(l_4^2+n_3^2+n_4^2)\\&-1890l_3^2n_3^2-2940l_4^2n_3^4+5880l_3^4n_4^2+8820l_3^2l_4^2n_3^2-19\,110n_3^2n_4^2l_3^2]\\&+x_4l_3n_4(-690+4830n_3^2+2940l_4^2+630n_4^2-11\,760l_3^2l_4^2+3920l_3^2n_4^2+14\,700l_4^2n_3^2-16\,170n_3^2n_4^2)\\&+x_4l_4n_3(-390+3990l_3^2-420n_3^2+2730n_4^2+2940l_3^2l_4^2-36\,750l_3^2n_4^2-980l_4^2n_3^2+5880n_3^2n_4^2)\ ,\end{aligned} \tag{B13}$$

and

$$T_5 \equiv l_3 n_3[3780-4263l_3^2-4557n_3^2-1295l_4^2-32\,305n_4^2-3430l_4^2(l_3^2+l_4^2)+25\,725l_4^2n_4^2+29\,155n_4^2(n_3^2+n_4^2)$$
$$+245l_4^2n_3^2+32\,830l_3^2n_4^2+3430l_4^4n_3^2-29\,155l_3^2n_4^4+30\,870l_3^2l_4^2n_4^2-56\,595n_3^2n_4^2l_4^2]$$
$$+l_4n_4[630-13\,720l_3^2+11\,620n_3^2-588l_4^2-882n_4^2+13\,720l_3^2(l_3^2+l_4^2+n_4^2)$$
$$-13\,720n_3^2(l_4^2+n_3^2+n_4^2)-7350l_3^2n_3^2+13\,720(l_4^2n_3^4-l_3^4n_4^2)-20\,580l_3^2l_4^2n_3^2+72\,030n_3^2n_4^2l_3^2]$$
$$+x_4l_3n_4(4550-3920l_3^2-20\,090n_3^2-6860l_4^2-8330n_4^2+27\,440l_3^2l_4^2-34\,300l_4^2n_3^2+58\,310n_3^2n_4^2)$$
$$+x_4l_4n_3(-350-9310l_3^2+3920n_3^2+980l_4^2-490n_4^2-6860l_3^2l_4^2+85\,750l_3^2n_4^2-27\,440n_3^2n_4^2)\ . \quad \text{(B14)}$$

Equations (B4)–(B14) can be applied to configurations (b) and (c) of Fig. 6 by replacing x_1, x_2, x_3, x_4, x_5, and x_6 by x_7, x_8, x_9, x_{10}, x_5, and x_{12}, respectively, for configuration (b) and by x_{11}, x_{12}, x_5, x_6, x_3, and x_4, respectively, for configuration (c).

Although algebraically complicated, Eq. (B4) for the four-ion angular function M is nonetheless exact and computationally very efficient. Whenever additional symmetry exists in a given four-ion interaction, the form of M can usually be greatly simplified. In the case of coplanar interactions with $r_1=r_2=r_4=r_5$, Eq. (B4) reduces to Eq. (53) for configuration (a) of Fig. 6 and to Eq. (54) for configuration (b) or (c), as indicated in Sec. III A. Similarly, in the case of out-of-plane interactions with $r_1=r_2=r_4=r_5$ and $\theta_2=\theta_4=\pi/2$ for configuration (a), Eq. (B4) becomes

$$M(x)=\tfrac{1}{5792}(-258+4830x^2+330y^2-26\,625x^4+8430x^2y^2+1125y^4+41\,580x^6-35\,490x^2y^4$$
$$-14\,490x^4y^2-420y^6-17\,395x^8+16\,660x^2y^6-53\,655x^4y^4+53\,410x^6y^2+980y^8)\ . \quad \text{(B15)}$$

with $\theta=\theta_1=\theta_3$, $x=\cos\theta$, and $y=1-x$.

[1] W. A. Harrison, *Pseudopotentials in the Theory of Metals* (Benjamin, New York, 1966).

[2] V. Heine and D. Weaire, in *Solid State Physics,* edited by F. Seitz, D. Turnbull, and H. Ehrenreich (Academic, New York, 1970), Vol. 24, p. 249.

[3] L. Dagens, M. Rasolt, and R. Taylor, Phys. Rev. B **11**, 2726 (1975).

[4] J. A. Moriarty, Int. J. Quantum Chem. Symp. **17**, 541 (1983).

[5] J. Hafner, *From Hamiltonians to Phase Diagrams* (Springer, Berlin, 1987).

[6] J. A. Moriarty, Phys. Rev. B **5**, 2066 (1972).

[7] J. A. Moriarty, Phys. Rev. B **16**, 2537 (1977); **26**, 1754 (1982).

[8] P. Hohenberg and W. Kohn, Phys. Rev. **136**, B864 (1964); W. Kohn and L. J. Sham, *ibid.* **140**, A1133 (1965).

[9] L. Hedin and B. I. Lundqvist, J. Phys. C **4**, 2064 (1971).

[10] J. A. Moriarty, Phys. Rev. B **38**, 3199 (1988).

[11] J. A. Moriarty, in *Many-Atom Interactions in Solids,* edited by R. Nieminen, M. J. Puska, and M. Manninen (Springer, Berlin, in press).

[12] Note that in the present paper we use $E_{\rm vol}$ to denote the volume term in the *cohesive energy* $E_{\rm coh}$, whereas in Ref. 10 $E_{\rm vol}$ denotes the volume term in the *valence-binding energy* $E_{\rm bind}$.

[13] O. K. Andersen, Phys. Rev. B **12**, 3060 (1975); O. K. Andersen and O. Jepsen, Physica B+C (Amsterdam) **91B**, 317 (1977).

[14] D. G. Pettifor, J. Phys. F **7**, 613 (1977).

[15] H. L. Skriver, *The LMTO Method* (Springer, Berlin, 1984).

[16] J. E. Lennard-Jones, Proc. R. Soc. London, Ser. A **106**, 463 (1924). In the rare-gas solids, of course, the physical origins of the terms in the Lennard-Jones potential are viewed rather differently. In that case, the repulsive r^{-12} term is intended to represent the hard-core-like interaction we have included in $v_{\rm hc}$, while the attractive r^{-6} term is intended to represent the van der Waals interaction arising from dipole-dipole coupling.

[17] J. A. Moriarty (unpublished).

[18] B. M. Axilrod and E. Teller, J. Chem. Phys. **11**, 299 (1943).

[19] J. A. Moriarty, J. Phys. F **5**, 873 (1975).

[20] C. Kittel, *Introduction to Solid State Physics,* 5th ed. (Wiley, New York, 1976), p. 74.

[21] D. L. Davidson and F. R. Brotzen, J. Appl. Phys. **39**, 5768 (1968).

[22] K. Maier, M. Peo, B. Saile, H. E. Schaefer, and A. Seeger, Philos. Mag. A **40**, 701 (1979).

[23] I. A. Schwirtlich and H. Schultz, Philos. Mag. A **41**, 91 (1980).

[24] R. Ziegler and H. E. Schaefer, in *Vacancies and Interstitials in Metals and Alloys,* edited by C. Abromeit and H. Wollenberger (Trans Tech, Aedermannsdorf, Switzerland, 1987), p. 145.

[25] A. R. Miedema and A. K. Niessen, CALPHAD **7**, 27 (1983).

[26] B. M. Powell, P. Martel, and A. D. B. Woods, Can. J. Phys. **55**, 1601 (1977).

[27] R. S. Hixson, D. A. Boness, J. W. Shaner, and J. A. Moriarty, Phys. Rev. Lett. **62**, 637 (1989).

[28] J. A. Moriarty (unpublished).

[29] The self-consistent LMTO calculations on fcc and bcc Mo (Refs. 10, 27, and 28) have been carried out within the usual nonrelativistic LDA framework (Ref. 8) using the Hedin-Lundqvist exchange-correlation potential (Ref. 9). The calculations employ the atomic-sphere approximation, the combined-correction term to this approximation, *s*, *p*, *d*, and *f* angular-momentum components of the valence-electron density, and the electrostatic Ewald or muffin-tin correction in the cohesive energy. The bcc-fcc and hcp-fcc structural energy differences have been obtained from the Andersen force theorem (Ref. 13) using the fcc electron potentials.

[30] K.-M. Ho, C.-L. Fu, and B. N. Harmon, Phys. Rev. B **29**, 1575 (1984).

[31] Y. Chen, C.-L. Fu, K.-M. Ho, and B. N. Harmon, Phys. Rev.

B **31**, 6775 (1985).
[32]N. Saunders, A. P. Miodownik, and A. T. Dinsdale, CALPHAD **12**, 351 (1988).
[33]H. L. Skriver, Phys. Rev. B **31**, 1909 (1985).
[34]L. F. Mattheiss and D. R. Hamann, Phys. Rev. B **33**, 823 (1986).
[35]C. T. Chan, D. Vanderbilt, S. G. Louie, and J. R. Chelikowsky, Phys. Rev. B **33**, 7941 (1986).
[36]Y. K. Vohra and A. L. Ruoff (unpublished); Y. K. Vohra (private communication).
[37]K. W. Katahara, M. H. Manghnani, and E. S. Fisher, J. Phys. F **9**, 773 (1979).
[38]J. A. Moriarty (unpublished).
[39]M. S. Daw and M. I. Baskes, Phys. Rev. B **29**, 6433 (1984).
[40]K. W. Jacobsen, J. K. Nørskov, and M. J. Puska, Phys. Rev. B **35**, 7423 (1987).
[41]J. C. Slater and G. F. Koster, Phys. Rev. **94**, 1498 (1954).
[42]W. A. Harrison, *Electronic Structure and the Properties of Solids* (Freeman, San Francisco, 1980), p. 481.
[43]We use the convention that $\mathbf{R}_{ij} \equiv \mathbf{R}_j - \mathbf{R}_i$, the vector from site i to site j. This is consistent with our notation for interatomic distances in the main text since $|\mathbf{R}_{ij}| = |\mathbf{R}_j - \mathbf{R}_i| = |\mathbf{R}_i - \mathbf{R}_j| \equiv R_{ij}$.